ABSTRACT

Title of Document: EFFECT OF LOAD HISTORY ON OVINE INTERVERTEBRAL DISC BIOMECHANICS

Addison Shay Goodley, M.S. 2014

Directed By: Professor Adam H. Hsieh,
Fischell Department of Bioengineering

Loading of the intervertebral disc (IVD) alters biomechanical properties by modifying fluid distribution in the nucleus pulposus –changing hydrostatic pressure and tissue response– during force transmission along the spine. This study combines pressure, vertical displacement, and radial bulge measurements to assess biomechanical function during healthy and adverse loading of ovine lumbar motion segments. High compressive loads and simultaneous transient exertions, representative of obesity or other high-load lifestyles, are expected to limit fluid recovery and inhibit IVD biomechanical function compared to low compressive load controls with similar transient exertions. Specifically, the adverse group will (1) lose the ability to generate intradiscal pressures equivalent to control discs at equal loads and (2) exhibit a greater degree of deformation and bulge during comparable loading. This study contributes a greater understanding of the effects of load on IVD health. Findings may inform future efforts to preserve disc biomechanics and reverse IVD loss of function.

EFFECT OF LOAD HISTORY ON OVINE INTERVERTEBRAL DISC BIOMECHANICS

By

Addison Shay Goodley

Thesis submitted to the Faculty of the Graduate School of the
University of Maryland, College Park, in partial fulfillment
of the requirements for the degree of
Master of Science
2014

Advisory Committee:
Professor Adam H. Hsieh, Chair
Dr. Maureen Dreher
Professor Steven Jay
Professor Miao Yu

Dedication

To my family.

Mom and Dad, thank you for your unwavering support and insightful guidance in all that I do.

Daniel and Grace, thanks for being there for me when I need a laugh and a break from it all.

If I wanted to get work done, I could not go home for a weekend, knowing that my family's endless love and their support of my enduring passion for the outdoors would distract me from accomplishing what I needed to do. It is a testament to my family that I am able to enjoy my time at home as a time spent away from work. For that I am ever grateful.

Acknowledgements

Thank you to…

My advisor, Dr. Adam Hsieh. Your guidance helped me to develop this project into what is presented herein while simultaneously cultivating my interest in biomechanics. I appreciate your attention to not only my research but also my plans for work outside of academia, and the occasional fishing story or two that I undoubtedly shared along the way.

My lab mates: Poonam, Joe, Lauren, Carlos, and Hyunchul. I appreciate your company during lab meetings, your ability to address my questions, and your willingness to share your experiences with me. Though they never seemed as often as Joe would prefer, happy hours at Looney's were always a good time. I wish all of you the best in your continued research.

My undergraduate assistant, Meghna. Without your help my research would have taken much more time and energy to complete. Thank you for your persistence with the pressure sensor construction and your uncanny ability to develop my scattered ideas into an intelligible final result.

The Sensors and Actuators lab. Hyungdae, your time and patience spent bringing me up to speed –and assistance throughout the duration of this project– is greatly appreciated. Dr. Yu, I hope that the same interdisciplinary collaboration that enabled the success of this research will continue as a mutually beneficial research pipeline between the mechanical and bioengineering disciplines. An extended thank you for your willingness to serve as a member of my committee.

The Bioengineering Department. Dr. Peter Kofinas first presented me with the idea and opportunity to continue my studies as a Masters student early on as an undergrad, advice which I am very much grateful for. Tracy Chung and the rest of the department's staff always impressed me with their speedy response and friendly smiles regardless of my request.

My committee members: Dr. Maureen Dreher, Dr. Adam Hsieh, Dr. Miao Yu, and Dr. Steven Jay. A warm thank you for accepting the responsibility of evaluating my research and challenging my findings. I appreciate your contributions, insight, and commitment to further improve this body of work.

My family and friends. A large thank you to Gretchen for your unwavering help and support up to the final edits of this thesis, to Kris for your patience when I was too tied up with my studies to throw the football or Frisbee, and to all of those whose unmentioned thoughts and prayers enabled me to complete this degree. Your love will continue with me as I move onward to my next adventure.

Table of Contents

List of Tables

List of Figures

Chapter 1: Introduction

1.1 Anatomy and Function of the Intervertebral Disc

The intervertebral disc (IVD), a soft tissue which supports and transfers loads between the vertebrae of the spine, is comprised of an inner nucleus pulposus and an outer annulus fibrosis. The nucleus pulposus (NP) is the gelatinous core with a high concentration of hydrophilic, poly-anionic proteoglycans to attract and retain water for uniform force dispersion. The annulus fibrosus (AF) is a layering of approximately 15-20 lamellar sheets which form a lattice of concentric layers enclosing the NP (Whatley et al., 2012). Intervertebral discs interface with each vertebra at a water-permeable cartilaginous structure called the vertebral endplate (Figure 1).

The NP region is predominately designed to withstand compressive loading and preserve the structural integrity of the disc. The extracellular matrix, produced by an estimated 4 $x10^6$ to $6x10^6$ cells/ml within the NP (Cassinelli et al., 2000; Maroudas et al., 1975), is responsible for bearing a high percentage of the total NP load. Proteoglycans like aggrecan, which contain many glycosaminoglycan (GAG) attachments for enhanced water attraction, account for ~50% of the NP dry weight. They are comprised of negatively charged brush-like structures which function to attract positively charged cations (Cassinelli et al., 2000). Attracted cations and their respective counterions, increase local ionic concentrations within the aggrecan rich NP. High ion concentrations induce an influx of water molecules to equilibrate osmotic pressures (Figure 1C). This aggrecan-induced osmotic pressure plays a critical role in resisting compressive loads, until age, injury, degradative enzymes, or load history alter the aggrecan structure or

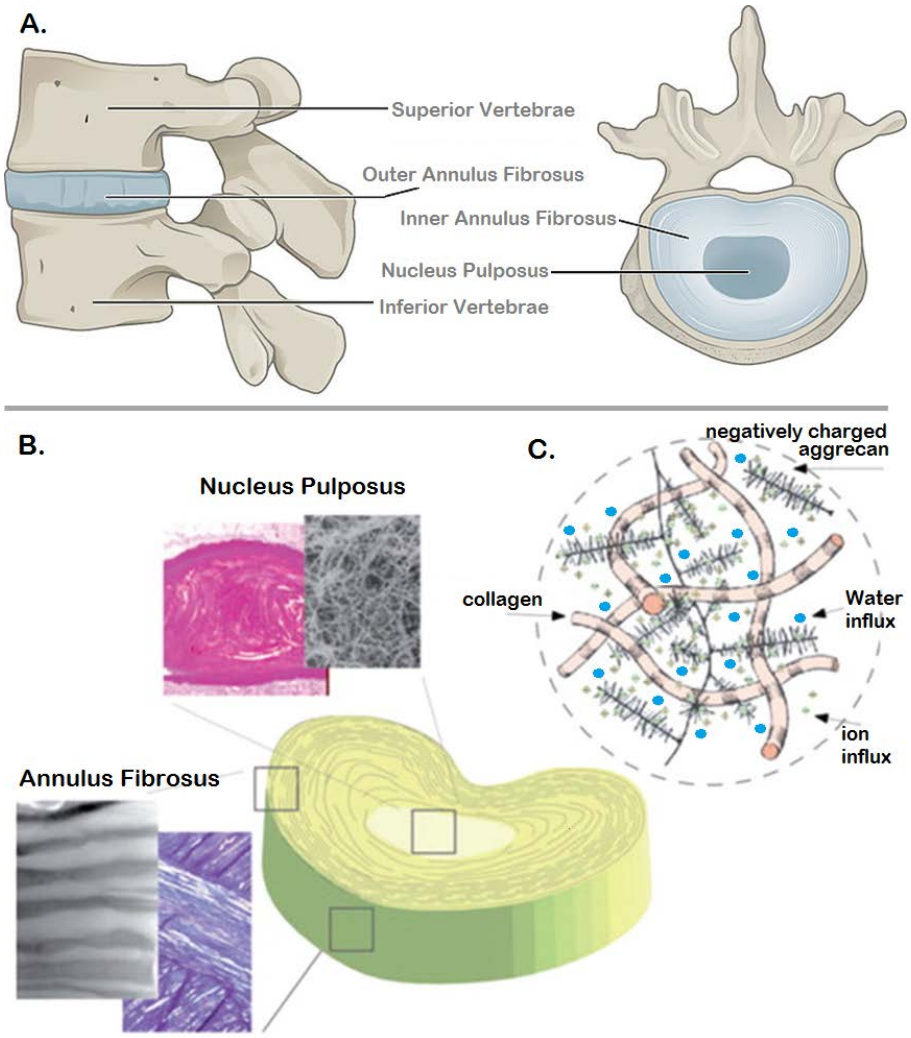

Figure 1: Structure of the IVD. Anatomical location of the IVD with respect to vertebrae (A), histology and brightfield images of annulus fibrosus and nucleus pulposus (B), and molecular level schematic of osmotic pressure generation within the IVD (C). Negatively charged aggrecan molecules attract cations associated with anion counterions. High local ion concentration generates influx of water to preserve osmotic pressure. Image adapted from Whatley et al. 2012; OpenStax, 2014.

fluidic environment within the NP. Unlike the water-attracting proteoglycans which function to resist compressive loads, the NP also contains type II collagen (~25% NP dry weight) which is thought to provide tensile strength to the NP (Cassinelli et al., 2000). Other collagen types and proteins within the NP further organize the structure of the IVD's gelatinous core and account for the remaining percentage of NP dry weight (Whatley et al., 2012).

The AF is a complex of two concentric regions of collagenous lamellae designed to resist tension caused during NP deformation under compressive loading (Figure 1A, B). The outer annulus is comprised of densely packed, highly organized type I collagen fibrils (75-90% dry weight) which act to retain all tissues internal to the IVD. At a position closer to the center of the disc, the inner annulus is comprised of type I collagen (40-60% dry weight), and an increasing percentage of proteoglycans (20-30% dry weight) relative to the outer annulus (Whatley et al., 2012). The inner annulus loses the highly structured lamellar layers and becomes less dense closer to the NP. The inner AF is separated from the NP region by a transition zone where high concentrations of collagen in the AF give way to elevated proteoglycan concentrations characteristic of the NP. The transition zone is less organized, and the lamellae even less structured, than the inner AF and acts as an intermediary region between the NP and the AF.

Region	Outer Annulus Fibrosus	Inner Annulus Fibrosus	Nucleus Pulposus
Proteoglycan	< 20% dry weight	20-30% dry weight	50% dry weight
Collagen	Type I; densely packed and highly organized 75-90% dry weight	Type I; less dense and less organized 40-60% dry weight	Type II; 25% dry weight

Table 1: IVD composition by region. Dry weight proteoglycan and collage percentages from the major regions of the disc. Note that proteoglycan percentages increase in regions central to the disc, while collagen is more prevalent in outer regions. Dry weights for proteins and less prevalent collagen types involved in maintenance of structure and organization are not included in this table.

The vertebral endplates serve as the attachment point between the lamellae of the AF and the cortical bone of the vertebral body. The endplate is predominantly hyaline cartilage, reportedly 600-800 microns thick across all lumbar vertebrae, and functions to contain the NP region during loading and enable fluid exchange for nutrient transport

(Moon et al., 2013). Since the IVD is largely avascular, nutrient transfer via fluid exchange is the predominant delivery mechanism. However, during aging, degeneration, or injury, endplates may calcify or otherwise exhibit reduced porosity leading to low permeability and reduced nutrient exchange (Wu et al., 2013). The distinct components of the IVD work together to maintain the fluidic NP environment which enables the spine to support compressive loads while also providing a mechanism for nutrient exchange.

IVDs function as ligaments to hold adjacent vertebrae together and act as joints to enable bending and rotation of the torso. They also play an integral role in load transmission along the spine (Whatley et al., 2012). When compressive force is applied, the hydrated NP is compressed and pressurizes. During this compression, water is expelled from the NP when aggrecan-induced osmotic pressure is overcome by hydrostatic pressure generated by NP deformation. This expelled water enters the AF's inter-lamellar space and passes across the vertebral endplates. Upon removal of load, NP hydration levels return with load and rate dependencies (Johannessen et al., 2004; O'Connell et al., 2011).

IVD biomechanics have been shown to change with age, genetics, and load history, but these factors can ultimately be related back to disc hydration. The concentration of aggrecan is known to decline beginning in the early twenties, reducing the maximum osmotic pressure and limiting IVD resistance to load (Sivan et al., 2014). Genetic factors controlling extracellular matrix production, GAG structure, and proteoglycan-degrading enzymes are also shown to contribute to large variations in disc health (Kepler et al., 2013). Loading experiments, characterized by high load magnitudes or excessive range of motion, demonstrate tissue dehydration and loss of aggrecan structures (McMillan et al.,

1996; Walter et al, 2011). The enclosed work describes the effect of load history on IVD hydration by observing tissue response to compressive loads in a sheep model.

1.2 Competing Factors in Disc Health

1.2.1 Effect of Age on Disc Health

A number of definitions explain lower back pain in relation to age effects and disc degeneration. De Schepper (2010) proposed age-dependent disc space narrowing was a causal factor for lower back pain, according to human lumbar radiographs. The study reported increased disc space narrowing was associated with increased age, and narrowing at two or more levels was associated with lower back pain more often than narrowing at a single level (De Schepper et al., 2010). Twomey et al. (1985) showed that increase in age alone does not cause decrease in disc height. Instead, reduced patient height and spine length in the elderly is often due to loss of transverse trabeculae of lumbar vertebrae (end plate collapse) as discs “sink” into the vertebrae (Twomey et al., 1985).

Disc thinning contributes to patient height loss only when disc degeneration occurs; however, disc degeneration does not always translate to disc thinning (Nachemson et al., 1979). Twomey et al. (1985) acknowledged two causes of disc thinning: loss of disc material due to herniation and volume loss from dehydration. Herniation events are often sudden and severe, and unlikely to trigger only slight reduction in volume during aging. This suggests fluid loss as a mechanism of disc thinning. Adams et al. (1996) observed fluid loss in aged discs by monitoring disc hydrostatic pressure. The study noted hydrostatic pressure loss of up to 30% between young and aged discs, and also documented up to 50% reduced NP size in aged tissues.

As the NP changed, so too did the force distribution within the disc (Adams et al., 1996). Stress profiling of age-degenerate discs demonstrated non-uniform pressure distributions and elevated peak pressures within the AF.

A closer look into the aging process of IVDs shows reduced functionality of the NP to attract and hold water. Aging has been related to the shifting of the NP from a gel-like tissue to a fibrous, less fluid region (Buckwalter, 1995; Livshits et al., 2011). Antoniou et al. (1996) reported significantly lower water content in the nucleus of mature, aged donors versus donors <25 years of age. In populations aged >30 years, NP water content was further reduced in samples with greater degrees of disk degeneration. For increasing degeneration, water content increased in the surrounding AF respective to the NP. The study also reported reduced GAG concentrations in populations >25 years of age (Antoniou et al., 1996). GAGs, long negatively-charged polysaccharide chains stemming from proteoglycans, are known to recruit water for tissue hydration and have been shown to decrease in concentration along the radial direction of healthy IVDs (Saar et al., 2012). Loss of GAGs in the nucleus in aged populations suggests a lower capacity to recruit and hold water within the NP. In the oldest age group (60-80 years), Antoniou et al. showed that uniform GAG distribution profiles across the NP and AF regions of the discs were present. Additionally, this study showed that increased GAG loss from the NP was associated with higher levels of disc degeneration, independent of age (Antoniou et al, 1996). GAG distribution is critical to maintaining high water content in the NP: reduced GAG concentrations and loss of associated water compromise the spine's natural load-bearing mechanism.

Adams et al. (2006) suggests disc degeneration is caused by uncontrollable genetic factors, in addition to nutritional imbalances, load history, and aging. Age is not the sole causal factor of disc degeneration, but the aging process does play an established role in the changing composition of the IVD. Osteoporotic vertebrae cause endplate collapse and subsequent disc space narrowing. Forces transmitted down the spine pressurize the NP and expel water from the tissue. Age-related loss of GAGs, and the gel-like to fibrous transition within the NP, limit the hydration and viscoelasticity of the NP region. Aging is a naturally unstoppable process, but understanding and reversing the effect aging has on NP water retention and fluid recovery is necessary to preserve IVD health.

1.2.2 Effect of Load History on Disc Health

Loading events condition the cells of the IVD and thus influence the tissue level; however, sustained compressive loads and repeated innocuous cycling can shift internal mechanics of IVDs such that subsequent loading events are detrimental to both cell and tissue function.

The diurnal cycle of spine loading ranges from pressures between 0.2MPa (at rest, supine) to 0.6MPa (upright posture, load bearing activity) with a frequency from 0.2-1 Hz (Chan et al., 2011). Loading within these physiological norms maintains cell and overall tissue health while exchanging as much as twenty-five percent of the disc's water content within a single 24 hour period (Sivan et al., 2006). Both adverse and neutral loading as well as complex asymmetric loading have been linked to IVD swelling, cell death, and disc degeneration (Stokes et al., 2004; Walsh et al., 2004; Wuertz et al., 2009; Walter et al., 2011). Individuals' daily activity, posture, and exercise also create a broad range of

unique spinal loading histories which must be considered when assessing the effect of load history on IVD health.

The cellular response (matrix synthesis and phenotypic shifts) reflects cells' interaction and feedback with their extracellular environment. Pairing RT-PCR with novel mechanisms for applying compressive forces to motion segments in vivo, up regulation of mRNA coding for anabolic and catabolic proteins can be correlated to loading profile (MacLean et al., 2005). Osmolarity has also been linked to altered gene and protein expression in IVD cells. Through different osmotic and mechanical loading conditions, extracellular environments affect expression of aggrecan and collagen, and thus subsequent IVD response to hydrostatic pressures and cyclic strains (Wuertz et al., 2007).

At the tissue level, osmotic pressures within IVDs play a key role in supporting applied loads. During loading, fluid displacement from the NP, endplate, and AF modifies disc biomechanics. Axial ramp and creep loading data from human lumbar spines match with rheological modeling suggesting fast fluid flow through the NP and endplate, and a slow response in the AF (O'Connell et al., 2011). MRI imaging shows similar water loss after axial fatigue testing (Yu et al., 2003). The expulsion of fluid reduces the gel-like character of the disc, and dehydration leads to a stiffer IVD. Ovine models demonstrate cyclic axial compression results in increased elastic stiffness as well as reduced total relaxation when compared to unloaded motion segments (Johannessen et al., 2004). Numerous studies have reported IVD biomechanical property changes with varied load histories, and just as many have investigated the restorative rehydration of preloaded tissues and the recovery of initial biomechanical properties after loading.

Recovery is a time, load, and fluid flow dependent process. Ovine disc experiments observed full return of disc stiffness and stress-relaxation properties after removal of all loads and submersion in PBS for 18 hours (Johannessen et al., 2004). Others have paired *ex vivo* testing with rheological spring-and-dashpot models to quantify recovery rates. Eight hours after a 2000N compressive ramping load, human discs returned to within 5% of the initial linear-region stiffness and disc height. The same study also investigated recovery following a 4 hour, 1000N creep load, reporting the recovery response (over 24 hours at 20N applied load) between 44 and 98 percent, though these numbers were for healthy and degenerate discs, combined. The reported recovery in displacement from initial at equilibrium (after 15 and 24 hours) was modeled at about 0.3mm, or 86% recovery from a max displacement of 2.09mm at the conclusion of creep tests (O'Connell et al., 2011).

1.3 Role of Pressure Sensing in IVD Biomechanical Assessment

Fluid distribution within the disc has been shown to indicate disc health. A highly fluidic NP enables maximum pressurization for elevated resistance to compressive loads. Similarly, fluid expelled during loading, and recovered after, enables nutrient transfer to sustain the cells of the IVD. Until recently, fluid presence was measured by freezing tissues immediately after exposure to a load or other experimental treatment. After slicing, tissues were weighed before and after freeze drying (McMillan et al., 1996). Recently, miniaturized pressure sensors have enabled real-time observation of intradiscal pressures correlating to intradiscal fluid presence (Wilke et al., 1999; Claus et al., 2008; Adams et al., 1996; Vergroesen et al., 2014). Wilke et al. (1999) tracked in vivo pressure measurements from a human lumbar IVD during daily activities for a 24 hour period. Just

as fluid was expected to return during diurnal resting cycles, pressure also increased (Wilke et al., 1999). Similarly, the percentage of water was shown to be highest within the NP and dissipate with radial position in the AF (Whatley et al., 2012); pressure measurements in human lumbar spines confirm fluid pressures were highest in the NP and tapered off in the AF (Adams et al., 1996). Pressure measurements allow the fluid distribution within the disc to be monitored, and require only proper sensor placement to elucidate pressures within site specific locations throughout the disc.

Often, pressure sensors are inserted into tissue using a needle, yet needle puncture is also commonly used to induce degeneration within in vivo models (Michalek et al., 2010). Innovative microfabrication and designs enable smaller sensors for minimally invasive measurements and smaller delivery needles. Studies investigating the impact of needle size on disc biomechanics suggest that needles with a diameter less than one-quarter the disc height induce minimal difference in the disc's typical response to load (Elliot et al., 2008; Hwang et al., 2012). Careful consideration of specimen disc height relative to the geometry of pressure measurement devices is required to reliably measure tissue response and avoid confounding results from needle damaged tissue.

Our lab has previously demonstrated in vitro NP pressure measurements in rat caudal discs using miniaturized fiber optic pressure sensors (Nesson et al., 2008; Hwang et al., 2012). Motion segments were subjected to an 1800sec prestress load (either 0.05 or 0.3MPa) before a 900sec exertion load (0.5MPa) was applied. NP pressures recorded during the exertion phase were different between the two prestress groups. The 0.05MPa prestress group developed 0.5MPa of pressure during the exertion phase, while the 0.3MPa prestress group exhibited significantly reduced pressure during the same

equivalent exertion load. This reduced pressure generation, paired with conclusions describing the load-bearing role of the AF and implications of an elevated shear environment, suggest certain load histories may accelerate age-related changes to IVDs (Hwang et al., 2012). Hwang et al. provided a platform from which additional pressure measurement studies could develop. Changes to the pressure sensing system, the switch to larger, more relevant tissues, and a novel loading regimen were made such that this thesis research builds upon the fundamental understanding of the effects of load history on IVD biomechanics.

1.4 Objectives

Loading IVDs alters pressure, hydration, and inherent tissue response during, and after, force application. We aim to further demonstrate the loss of function and shift in biomechanics for different compressive loading regimens. We hypothesize high compressive loading with simultaneous transient exertion loads will alter fluid distribution, and thus biomechanical function, in sheep lumbar motion segments as compared to low compressive loading controls exposed to similar transient exertion loads.

To assess biomechanical function, pressure measurements as well as vertical and radial displacements were collected using a variety of instruments. A micro Fabry-Perot pressure sensor was designed to observe NP pressure. Axial displacement measurements were used in conjunction with disc heights to quantify disc strains. When the NP region is compressed under axial load, its volume expands in the radial direction to preserve initial NP volume. NP radial expansion is contained by the AF, which in turn also bulges radially. This phenomenon, described as disc bulge, has been studied as an indirect

measurement of NP pressure (Heuer et al., 2007; Pei et al., 2014). A number of disc bulge measurements were attempted in the preparation of this thesis.

In vitro mechanical tests of sheep lumbar motion segments were used for all data collection. Sheep lumbar motion segments –comprised of an intact IVD between respective superior and inferior vertebrae– have been validated and used commonly as biomechanical models of the human lumbar spine (Wilke et al., 1997; Smit et al., 2002). The enclosed findings provide additional understanding of the dynamics of short-term loading and recovery of intervertebral discs.

Further interpretation may provide physiological insight into load-induced biomechanical changes to guide clinical prevention and treatment of IVD degeneration and loss of function. Applied loads used in this study were representative physiological values: both high and low compressive resting loads represent physically relevant conditions. High resting loads can be compared to effects of obesity, heavy manual labor occupations, or other lifestyle choices which introduce prolonged, elevated compressive stresses to the spine. Increased loading magnitudes limit fluid recovery, but prolonged loads further restrict recovery such that elevated yet innocuous loads result in accumulated, damaging effects on disc biomechanics.

Chapter 2: Sensor Construction

2.1 Introduction

Fabry-Perot sensors are an established tool for reliable pressure measurement (Dakin et al., 1987; Wolthuis et al., 1991). Miniaturized versions have been used to measure intravenous and other low pressure biological environments, but until recently custom Fabry-Perot sensors capable of reading the relatively high physiologic pressures associated with intervertebral discs had not been developed (Poeggel et al., 2014; Nesson et al., 2008). Fiber optic sensors from commercial manufacturers like Opsens (Quebec, Canada) and Fiso (Quebec, Canada) measure relatively small pressures (up to 1MPa, though often 0.04MPa) and fell short of physiologic IVD pressure ranges. Signal artifact from fiber motion during pressure measurement has also been noted in commercial sensors. The companies' small-diameter sensors rated to measure high physiological pressures were larger in diameter (250-800μm) than the custom sensor design. Fiso's FOP-M series sensor exceeded physiological pressures (rated to 6+MPa) and despite an 800μm outer diameter, was also cost prohibitive: commercial signal conditioners and other components have considerable start-up costs associated with acquiring the full measurement system. Commercial sensors' inadequate specifications and high cost prompted continued development of custom sensors until the design suited IVD pressure measurement, exhibited less sensitivity to fiber motion, and were cost effective.

With assistance from Dr. Miao Yu and Dr. Hyungdae Bae (Sensors and Actuators Lab, University of Maryland) a low profile sensor suitable for high pressure ranges was established. Prior collaboration with the Sensors and Actuators Lab yielded a fragile

sensor prone to damage by the effects of hydration upon exposure to the aqueous environment inherent to IVDs. The methods by which the design was improved, and the current sensors were fabricated, are described below.

2.2 Splicing Fiber Optic Cable to Capillary Tube

A length of SMF-28E+ fiber (Fiber Instrument Sales, Oriskany, NY) was cleaved at one end and placed opposite of a cleaved, hollow capillary tube 30μm ID/150 μm OD (TSP030150; BGB Analytik, Alexandria, VA) in a Type-36 Sumitomo Electric fusion splicer (Sumitomo Electric, Research Triangle Park, NC). Low-power spattering arc was applied to clean the square ends of the fiber and capillary before alignment along the axis of the fiber core. After ensuring slight contact between the aligned fiber and capillary, the interface was fused using a splicing arc at the conditions listed in the table below. The arc power and arc duration values were manipulated so that the inner diameter of the capillary tube did not taper or otherwise deform while splicing arc was applied. Ideally, the capillary's 30μm inner diameter dimension was preserved to ensure maximal passage of light across the fiber-capillary interface. Excessively large arc power or arc duration values distorted the capillary geometry, while low arc power and arc duration resulted in insufficient splice strength.

Arc Property	Value
Arc Duration	00.70
Pre-fusion	00.00
Arc Gap	03.50
Overlap	12.00
Arc Power	0025

Table 2: Settings used to fuse capillary tube to the terminus of the optical fiber. Arc Duration and Arc Power inputs were manipulated to ensure proper fusion strength.

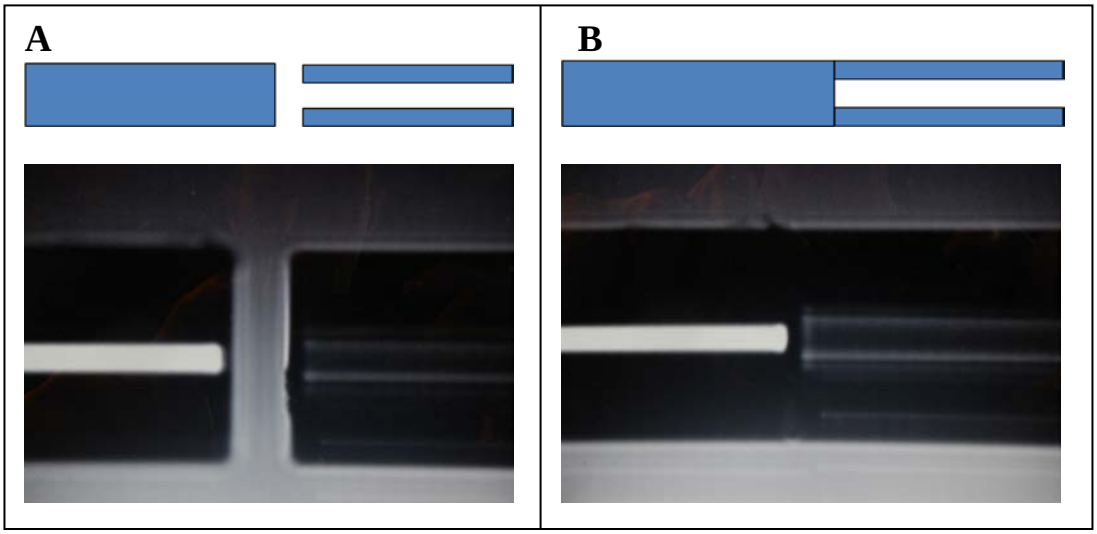

Figure 2: Side view of capillary/fiber after alignment (A) and fusion splicing (B) of capillary to optical fiber.

2.3 Cleaving the Capillary Tube and Enclosing the Cavity

Fabry-Perot cavity-based sensors measure the length of the sensor cavity to compute local pressure changes. Because of this, the inherent geometry of the cavity is important. After visually confirming the spliced capillary tube was cylindrical, the capillary tube was cut to proper length. Using a FC-6S fiber cleaver (Sumitomo Electric, Research Triangle Park, NC) beneath a 10x microscope, EO-3112C camera, and an MI-150 High Intensity Illuminator (Edmund Optics, Barrington, NJ) the spliced capillary tube was positioned with a 460A Series stage (Newport, Irvine, CA) and cleaved approximately 15μm from the spliced interface. The cleaved fiber-capillary was mounted on a glass slide until all units in the batch were cleaved.

To complete the cavity –and enclose the hollow space within the length of remaining capillary– a thin layer of UV curable polymer adhesive (OP-4-20641; Dymax, Torrington, CT) was applied to the capillary end opposite the spliced interface. A drop of polymer was allowed to spread on a surface of water to a thickness of 0.5μm. The polymer thin film was then half cured with a Model 22-UV light source (Optical

Engineering Inc., Santa Rosa, CA) before the capillary tubes were punched through the polymer film floating on the water's surface. The polymer affixed to the capillary was full-cured using additional UV light (BlueWave 50AS, Dymax UV Light Curing Systems, Torrington, CT). Presence of the polymer diaphragm was confirmed using a TMS-1200 microscope (Polytec, Irvine, CA).

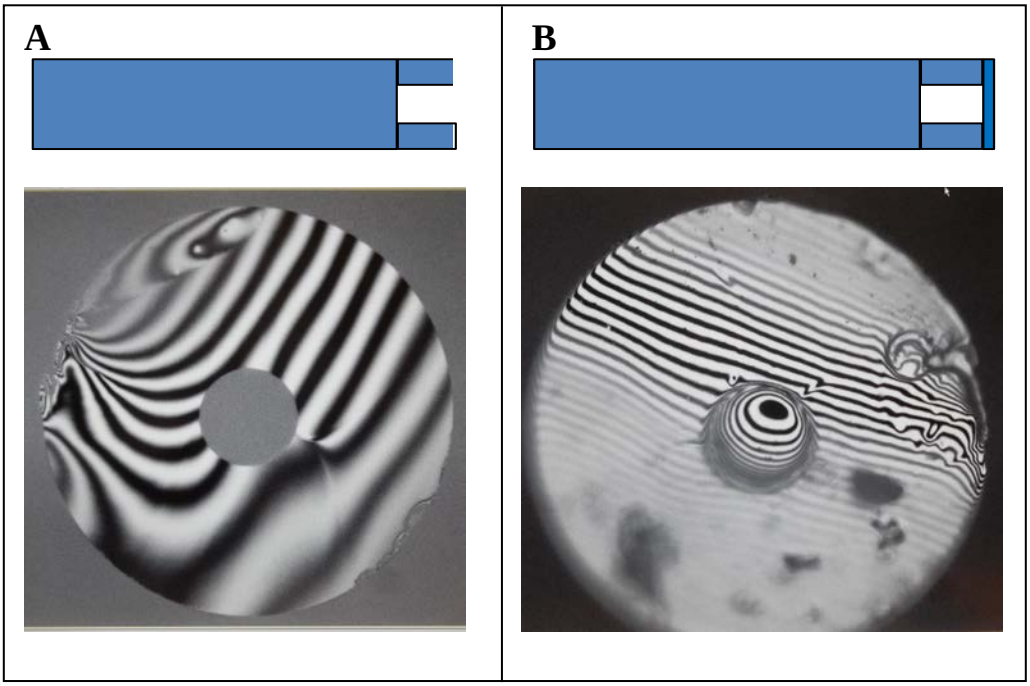

Figure 3: Sensor tip before (A) and after (B) addition of polymer layer. Striped patterning maps topography of sensor face. Note the cavity was enclosed after addition of the polymer.

2.4 Sputtering for Sensitivity

Fabry-Perot sensors measure cavity length, the length from the spliced fiber-capillary interface to the diaphragm enclosing the distal end of the capillary. The diaphragm deflects due to the environment surrounding the sensor tip, and deflection results in a changed cavity length. Thus, fluctuations of Fabry-Perot cavity lengths correspond entirely to diaphragm mechanical properties. Up to this step in the process of

sensor assembly, only a 0.5μm polymer diaphragm was present. To create a sensor rated for pressures associated with intervertebral disc loading (on the order of MPa) the design required an additional diaphragm layer to stiffen the sensor diaphragm. A bilayer diaphragm design was achieved by sputtering a layer of Titanium (Ti) onto the preexisting polymer layer. Ti was the metal of choice due to its corrosion resistance, biocompatibility, and overall common use as a biomaterial (Long et al., 1998).

An iterative process was used to establish the proper thickness of the diaphragm's metal layer. A balance between sensitivity and durability was required: thinner metal layers provided greater deflections at lower pressures for improved sensitivity and resolution, yet failed under physiologic pressures due to excessive deflection. Thicker metal layers provided a robust diaphragm design, but exhibited reduced sensitivity and limited resolution within the intended pressure range. Mathematical formulations were used to predict diaphragm behavior under anticipated pressure conditions and inform diaphragm geometries. Deflection (y) at the center of the diaphragm (r=0) was computed as the relationship between Poisson's ratio (μ) and Young's modulus (E) of the diaphragm materials as well as the applied pressure (P), and the radius (a) and thickness (h) of the diaphragm (MacPherson et al., 1999; Said et al., 2009).

$$y(r=0) = \frac{3(1-\mu^2)Pa^4}{16Eh^3} \qquad \text{Equation 2.1}$$

A standard practice in Fabry-Perot sensor construction is to limit the maximum diaphragm deflection to less than one fourth the value of the center wavelength (λ_o) of the illuminating light source (Chin et al., 2007).

$$y(r = 0) \leq \frac{\lambda o}{4}$$ Equation 2.2

Chin et al. (2007) provided additional guidance and outlined construction methods to further develop and characterize Fabry-Perot designs. The theory behind Equation 2.1 and Equation 2.2 was incorporated into ANSYS code developed by the Sensors and Actuators Lab (University of Maryland) and used to model bilayer diaphragm deflections to establish dimensions for the diaphragm.

Using outputs from ANSYS v14.5 (Cannonsburg, PA), a diaphragm with a radius of 15μm and thickness of 0.5μm Ti atop 0.5μm of polymer was attempted. Trial experiments in pressure chambers and disc tissues demonstrated that sensors with 0.5μm Ti were highly sensitive to pressure changes, but burst at physiological loads. Sensors with 0.6 μm Ti were fabricated and diaphragm bursting was eliminated. However, tissue testing and submersion tests in pressure chambers resulted in drifting pressure outputs, most likely due to water absorption. When 0.7μm Ti was sputtered atop a 0.5μm polymer layer, water absorption –and sensor drift– abated. The current sensor design uses a 700nm titanium metal layer atop the polymer diaphragm to provide a hydration resistant, sensitive, and reliable sensor. All titanium layers were sputtered in accordance with procedures listed in the Sensor and Actuators Lab (University of Maryland) at a deposition rate of 0.5 nm/sec.

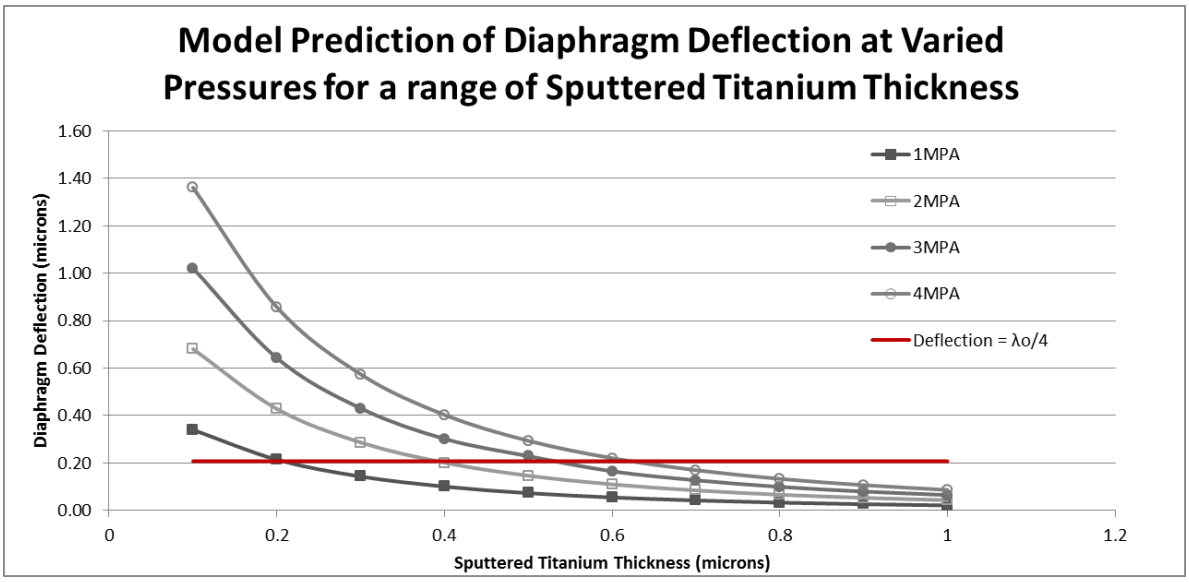

Figure 4: ANSYS deflection outputs for a bilayer diaphragm (15 micron radius, 0.5 micron thick polymer bottom layer) at physiologic loading pressures. Also included as a reference is the maximum deflection limit as defined by Chin et al. (2007) based on a center wavelength of 830nm from the light source.

2.5 Final Screening and Calibration

Sensors with a complete bilayer diaphragm were spliced to patch cords in order to connect the sensor to the spectrometer interrogation system. Using a LabView program adapted from the version currently used in the Sensor and Actuators Lab (University of Maryland) the fiber optic wavelength intensity signals was observed. Sensors with signals exhibiting distinct peaks of uniform width and height were selected and qualified for calibration testing.

Qualified sensors were calibrated in order to relate ambient pressure change to cavity length changes. A pre-existing calibration chamber in the Sensor and Actuators Lab (University of Maryland) was initially used to calibrate the sensors. The chamber provided consistent air pressure to 20psi (0.138MPa) but was well below the maximum design pressure of the sensors. It was expected that as long as the maximum diaphragm

deflection was 20-30% of the total diaphragm thickness, the deflection should be linear with increasing pressure. This enabled extrapolation of the 0-20psi calibration curve to the full rated pressure range of the sensor, but with such large scaling, there were concerns about the accuracy of the calibration data and the ability to extrapolate pressures to one order of magnitude larger than the experimental calibration pressures.

A custom calibration chamber was therefore developed, rated to over 400psi (3MPa), which was used to calibrate sensors over the entire designed-for pressure range. Pressure steps of 0.1MPa were used to characterize cavity length changes for pressures between 0.2MPa to 3.0MPa. All high pressure calibrations were conducted using compressed Nitrogen gas. A digital reference sensor (Model MG-500-A-9V-R, SSI Technologies, Janesville, WI) was used to confirm pressures within the chamber.

Sensors demonstrating low noise (±6nm cavity length), linear calibration curves, and return to initial cavity length upon return to zero pressure, were selected for use in the measurement of intradiscal pressures.

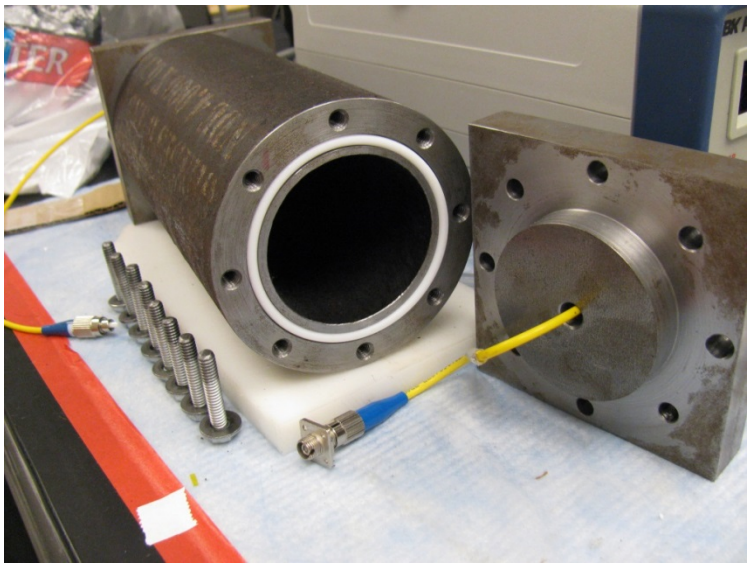

Figure 5: Custom calibration chamber. Compressed Nitrogen gas was used to calibrate sensors to 3MPa in both dry and wet (1X PBS in petri dish) conditions.

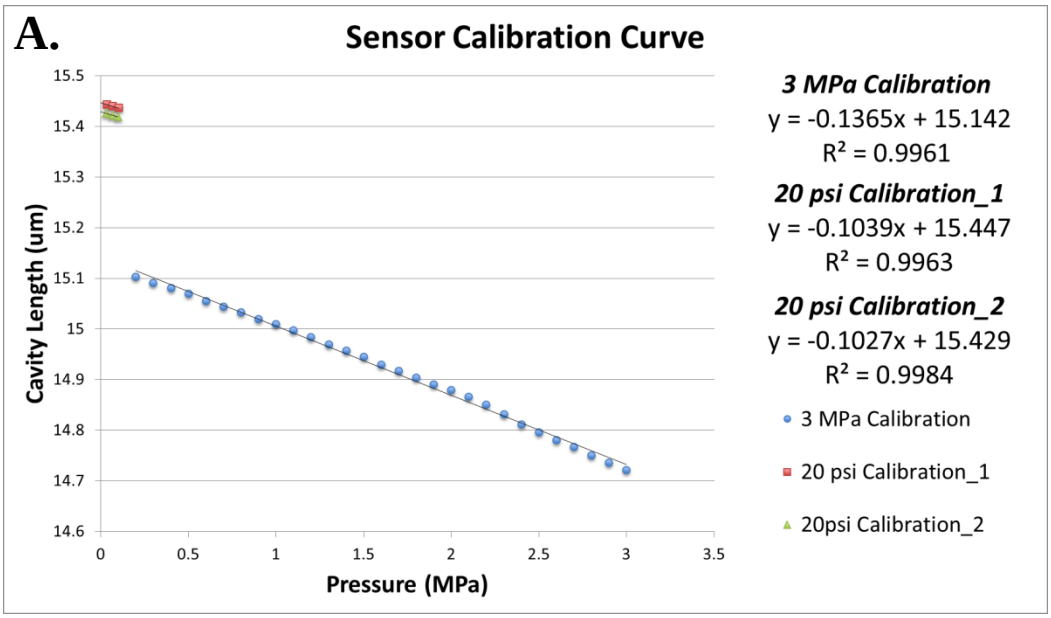

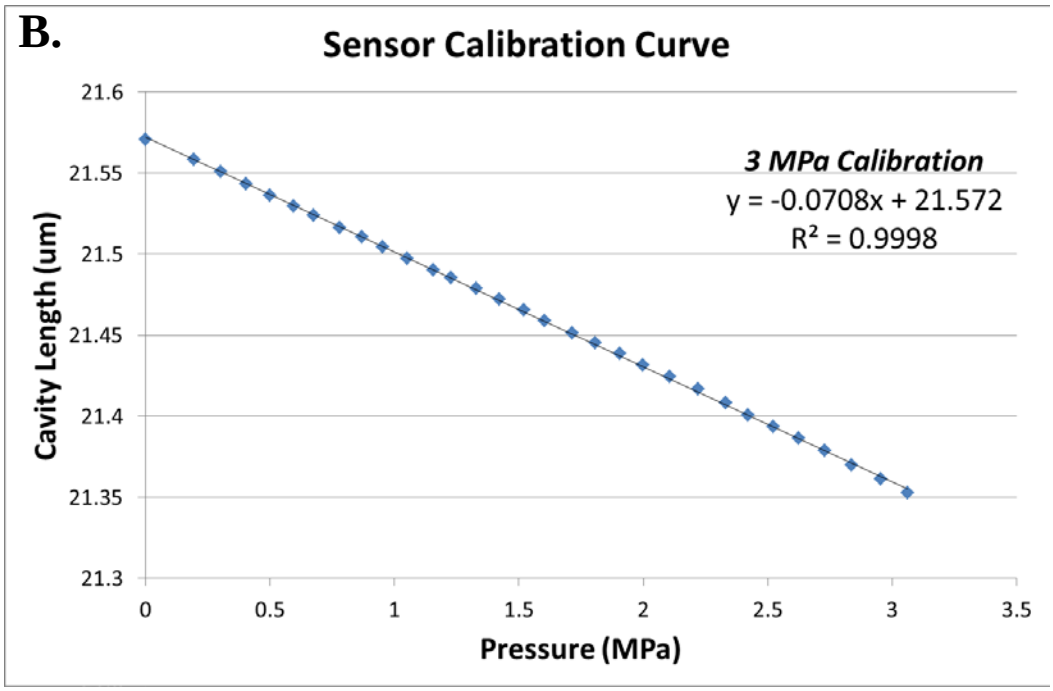

Figure 6: Calibration Curves. (A) Calibration curves for a single sensor in both calibration chambers (20psi, 3 MPa). It was common for the same sensor to report different initial cavity lengths during different experiments. However, to correlate the change in cavity length to a change in pressure, only the slope of the line was of interest. Only the slope of the 3 MPa calibration curve was used during all tissue testing. Note the total diaphragm displacement (change in Cavity Length) is approximately 0.4 microns after 3MPa applied pressure (A). The sensor used for (A) came from a batch using less than 0.7 micron titanium layer. Because of the thinner, more flexible diaphragm, slight inflection in the 3 MPa calibration curve is evident. Less inflection was observed in 3MPa calibration curves for sensors with 0.7 microns titanium (B).

Chapter 3: Influence of Load History on IVD Biomechanics

3.1 Introduction

The nucleus pulposus (NP) region of the intervertebral disc (IVD) contains approximately 70 to 90% water which functions to support compressive loading (Buckwalter, 1995; Iatridis, 1996, Whatley et al., 2012). Load history alters IVD biomechanical properties by modifying water distribution in the NP region, changing hydrostatic pressure and tissue response, when force is transmitted along the spine.

The effects that different loading profiles have on ovine IVDs were measured to elucidate the effects of load history on NP hydrostatic pressure and tissue response. Discs subjected to high recovery loads were expected to, as a result of limited fluid recovery, (1) lose the ability to generate equivalent intradiscal pressures and (2) exhibit a greater degree of deformation during comparable loading. This study contributes to a greater understanding of load effects on IVD pressure and health. Findings may also inform efforts to preserve disc biomechanics and reverse loss of disc function.

3.2 Methods

3.2.1 Specimen Preparation

Ovine lumbar motion segments (L2L3, L4L5) were harvested, surrounding tissues removed, wrapped in saline soaked gauze, and frozen (-20°C) until testing. Prior to testing, specimens were allowed to thaw overnight. Once thawed, cross-sectional areas of the disc were estimated by measuring disc long and short axis dimensions, and used to define an applied force required to generate target loading pressures. Preload disc height

was approximated using ImageJ (National Institutes of Health, Bethesda, MD) to interpret radiograph images from a FlouroScan III imaging system (FluoroScan Imaging Systems Inc, Northbrook, IL). Inferior vertebrae were potted into a custom fixture using Boswell Fastray Dental Cement (Bosworth Company, Skokie, IL) and a hole was drilled parallel to the frontal plane (approximately 3-5mm anterior to the vertebrae's center of mass) in the superior vertebrae so that forces applied to a rod slotted into the hole introduced a follower load in the motion segment. A rod was slotted through the superior vertebrae and the entire fixture was positioned in an 858 Mini Bionix II material testing system (MTS Systems Corporation, Eden Prairie, MN).

Altogether, ten sheep spines were acquired and twenty specimens were loaded, ten adverse and ten healthy, yet neither group had a 100% success rate as specimens slipped from the potting cement and pressure sensors broke or otherwise failed. From each sheep, L2-L3 and L4-L5 motion segments were harvested. Experimental design required each motion segment undergo just one loading regimen, and that segments from each sheep combine to receive one adverse and one healthy loading. The levels exposed to adverse and healthy loads were also intermixed so that differences between adverse and healthy loading groups were independent of level.

3.2.2 Mechanical Testing

Previous experimentation demonstrated that rat caudal discs pre-stressed at 0.05MPa for 1800sec generated greater intradiscal pressures than discs pre-stressed at 0.30MPa for 1800sec during equivalent exertion phases (Hwang et al., 2012). To better understand the effect of load history on intradiscal pressure generation, the current experiment divided motion segments into two groups to receive either a relatively high or

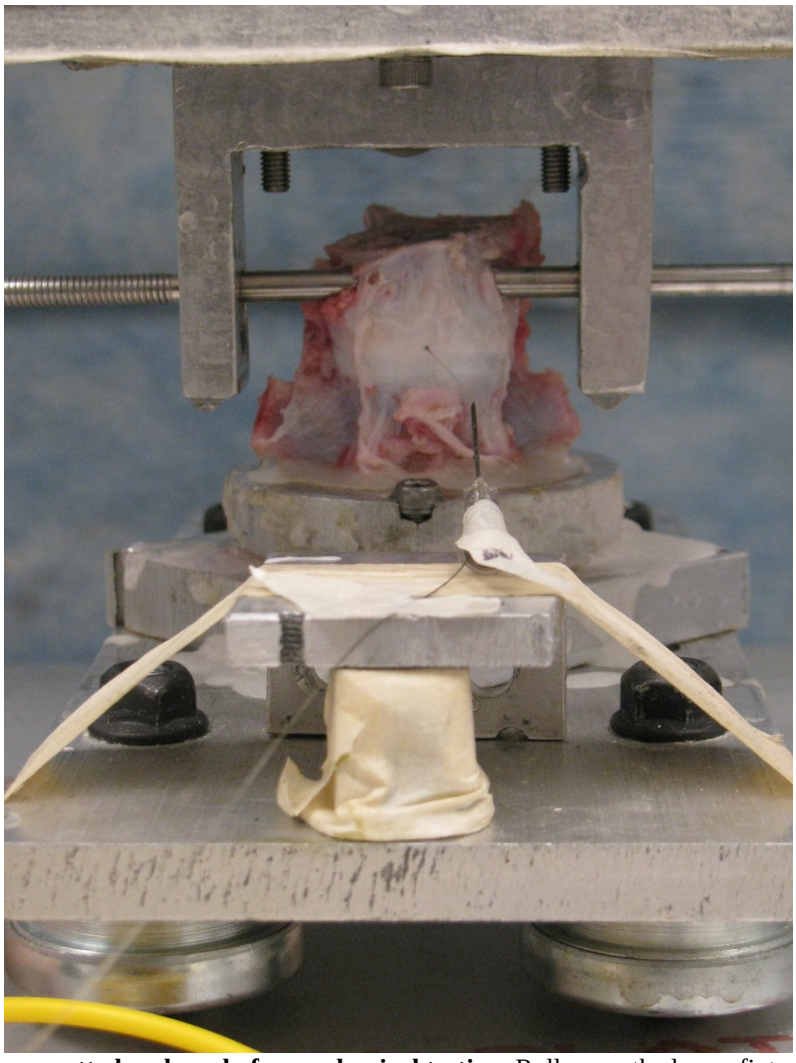

Figure 7: Specimen potted and ready for mechanical testing. Rollers on the lower fixture enable translational freedom. The load cell and actuator (above, out of view) were attached to the U-bracket (top) which engaged the motion segment when rod was slotted through pre-drilled holes in the superior vertebrae. Also pictured is the sensor (in place for testing) and needle used for sensor delivery.

neutral physiologic loading regimen and multiple short-term, high-load exertion challenges. Herein, the neutral loading profile is referred to as the "healthy loading group" with loads meant to simulate appropriate recovery between challenge loads. The high loading profile is referred to as the "adverse loading group" since the compressive loads applied between challenge loading were elevated from physiological resting levels.

The healthy group was subjected to a constant load of 0.05MPa (between 10N and 25N applied force) axial compression with seven transient 2MPa (between 600N and 1000N applied force) between challenge loads every 900sec. The adverse group received a constant axial compression load of 0.75MPa (between 200N and 400N applied force) with similar transient 2MPa challenge loads every 900sec. The 0.05MPa and 0.75MPa creep loads, referred to as recovery loads, were intended to replicate in vivo IDPs recorded during prone resting (0.05MPa) and standard loading (0.75MPa) activities (Sato et al., 1999; Wilke et al., 1999; Claus et al., 2008). Transient 2MPa challenge load exertions were meant to replicate high force challenges such as heavy lifting or other strenuous activity. Prior to testing, each motion segment was loaded in cyclic compression (0.05-0.25 MPa, 1Hz) to resolve any postmortem super-hydration effects (McMillan et al., 1996).

A miniature Fabry-Perot type pressure sensor was inserted into the anterior face of the disc to measure hydrostatic pressure in the NP. Sensors were guided by a 22 gauge

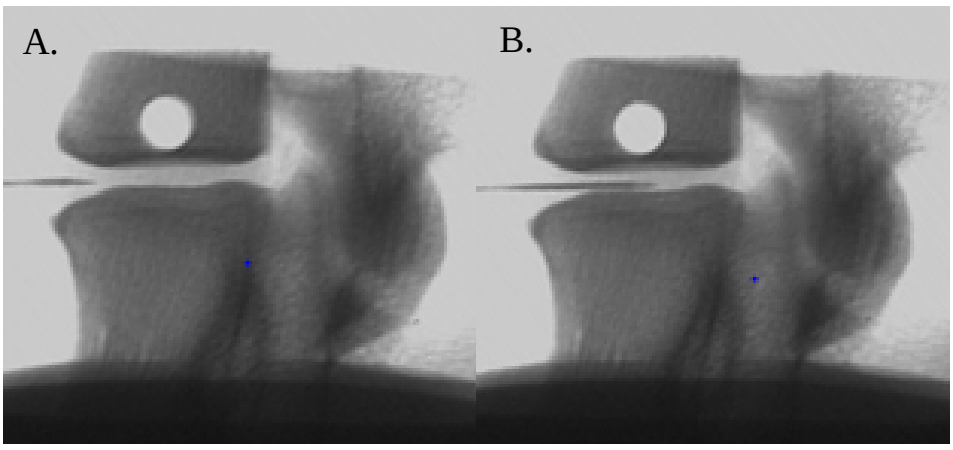

Figure 8: Verification of needle position. Lateral x-ray images were acquired to determine (A) initial placement and (B) penetration depth to precisely deliver the pressure sensor to the NP region.

needle into the center of the disc and positioning confirmed by radiograph. Needles were rescinded from the disc without disturbing the position of the sensor within the NP.

Disc bulge measurements were acquired using a Microtrak II laser triangulation device (MTI Instruments Inc, Albany, NY). Vertical scans of the disc at a lateral position 30° offset from the mid-sagittal plane were used to visualize the outer profile of the disc and superior and inferior vertebrae. Scans were conducted immediately before and after challenge loading events as well as 8 minutes after the conclusion of each challenge.

Axial displacement and force values were recorded by the MTS system at a frequency of 10Hz. Displacements were recorded as vertical position of the superior test fixture during testing.

At the conclusion of testing, disc radiographs were recorded and Image J was used to measure postload disc height.

3.2.3 Pressure Measurement

Custom Fabry-Perot pressure sensors were constructed by adapting fabrication methods presented by Bae (2012). A length of fiber optic cable (OD=150um) was spliced at one end to a capillary tube (ID=30um, OD=150um) ensuring the fiber core was aligned with the hollow center of the capillary. The spliced capillary was cleaved approximately 15um from the fiber interface and a 500nm thick UV curable polymer layer was added to the freshly cleaved capillary, enclosing the capillary cavity. A 700nm Titanium metal layer was sputtered onto the surface of the cured polymer to complete a flexible diaphragm atop the capillary cavity. Pressure changes at the capillary terminus cause the diaphragm to mechanically deflect so that changes in cavity length could be recorded and calibrated to quantify pressure at the sensor tip. All sensors were calibrated to 3MPa with

a reference pressure gauge (SSI Technologies Inc, Janesville, WI) in a custom calibration chamber. A fiber optic system (USB-4000 Spectrometer and HL-2000 Light Source, Ocean Optics, Dunedin, FL; Beam Splitter, Gould Fiber Optics) was used to record cavity length data at a frequency of 14.3Hz in LabView 2012 (National Instruments, Austin, TX). Signal optimization and processing were completed using MATLAB R2012b (MathWorks, Inc., Natick, MA).

3.2.4 Intradiscal Shear and Intradiscal Pressure Relation

Intradiscal shear (IDS) has been shown to influence NP cell phenotype and morphology (Wang et al., 2011). Previously, to better understand the existence and physiological ranges of IDS, a relationship was developed between observed NP pressure and IDS, using octahedral shear stress formulations and geometric assumptions for axisymmetric discs (Hwang et al., 2012). In the case of ovine lumbar IVDs, axisymmetric assumptions are not valid and further experimentation was required to validate key model assumptions. The following relation is developed from the definition of octahedral shear stress, where σ_1, σ_2, and σ_3 are the three principle stresses.

$$\tau_{octahedral} = \frac{1}{3}\sqrt{(\sigma_1 - \sigma_2)^2 + (\sigma_2 - \sigma_3)^2 + (\sigma_3 - \sigma_1)^2} \qquad \text{Equation 3.1}$$

If σ_1 is defined as the stress acting in the vertical direction, its value can be resolved as the stress applied to the NP, $\sigma_{applied_{NP}}$.

Spinal compressive forces are borne predominantly by the NP region of the IVD, such that stresses assumed to act over the entire disc cross section are not representative of the stress state within the NP. To control for the natural tendency of the NP to bear a

large percent of the overall compressive load, the total load applied to the disc was divided by the ratio of cross sectional areas, NP:Total Disc (O'Connell et al., 2007). This relation provides an estimate of stress applied to the NP based upon the NP cross sectional area relative to the whole disc, to better resolve the load borne specifically by the NP region.

$$\sigma_1 = \sigma_{applied_{NP}} = \frac{\sigma_{compression}}{\frac{Area_{NP}}{Area_{Disc}}} \qquad \text{Equation 3.2}$$

It makes sense that $\sigma_{applied_{NP}}$ is larger than the overall compressive load, since the NP represents only a small percentage of the disc's cross sectional area, but is responsible for resisting a large percentage of spinal compression.

The remaining two principle stresses, σ_2 and σ_3, come from pressures measured during in vitro testing. Sensors were inserted into the anterior and lateral faces of the IVD and positioned within the NP to observe pressures in the plane perpendicular to the direction of applied compression. Ovine disc geometries do not support prior assumptions of equal stress in all directions parallel to the plane perpendicular to the direction of applied compression, so additional experiments were conducted to understand the ratio between pressures acting orthogonal to the direction of applied compression. If compression is assumed to act in the z direction, the ratio between pressures measured in the x- and y-directions was used to relate experimental x-direction pressures (σ_2) to y-direction pressures (σ_3).

$$\sigma_2 = \sigma_{Pressure_X} \qquad \text{Equation 3.3}$$

$$\sigma_3 = \sigma_{pressure_x} \times \left(\frac{Pressure_y}{Pressure_x}\right) \qquad \text{Equation 3.4}$$

Substitution of the three principle stress values (Eqns 3.2, 3.3, 3.4) into the octahedral shear stress equation (Eqn 3.1) generates an estimate of intradiscal shear stress within the NP.

3.3 Results

To demonstrate changes in discs subjected to different load histories, vertical displacement, hydrostatic pressure, and radial budge data were recorded. Vertical displacement values were recorded as the displacement relative to the position at the conclusion of cyclic loading so as to eliminate effects caused by postmortem super hydration, but are also reported as percent strain values according to each specimen's respective preload disc height. Strain data was plotted with respect to time as a quasi-creep curve. Without transient challenges, the loading profiles represent classic creep experiments. Strain data were fit to a simple one-dimensional fluid transport model to uncover differences in tissue response to adverse and healthy loading conditions. NP pressures are similarly reported as the pressure difference respective to the end of cyclic preconditioning. NP pressures were used as a basis for computing estimates of intradiscal shear using an octahedral shear stress model. Disc bulge data are presented qualitatively as silhouette profiles, with vertical position normalized to approximate disc height.

Statistical differences, often observed between healthy and adverse groups, were assessed using two-tailed t-tests for which p-values less than 0.05 were accepted as significant.

3.3.1 Adverse loading increases axial strain

Changes in displacement between challenge loads within a single motion segment were statistically different ($p<0.03$) between healthy and adverse groups. From the first to the final challenge, healthy discs displaced -0.09 ±0.04mm while adverse discs displaced -0.58±0.34mm. Displacement values from each challenge were normalized to the initial challenge's displacement in which adverse discs displaced a significantly greater amount than healthy discs for all but the initial challenge ($p<0.05$).

Average disc height for each sheep was calculated from lateral radiographs using the mean of three heights recorded between the anterior corners of the vertebrae and three

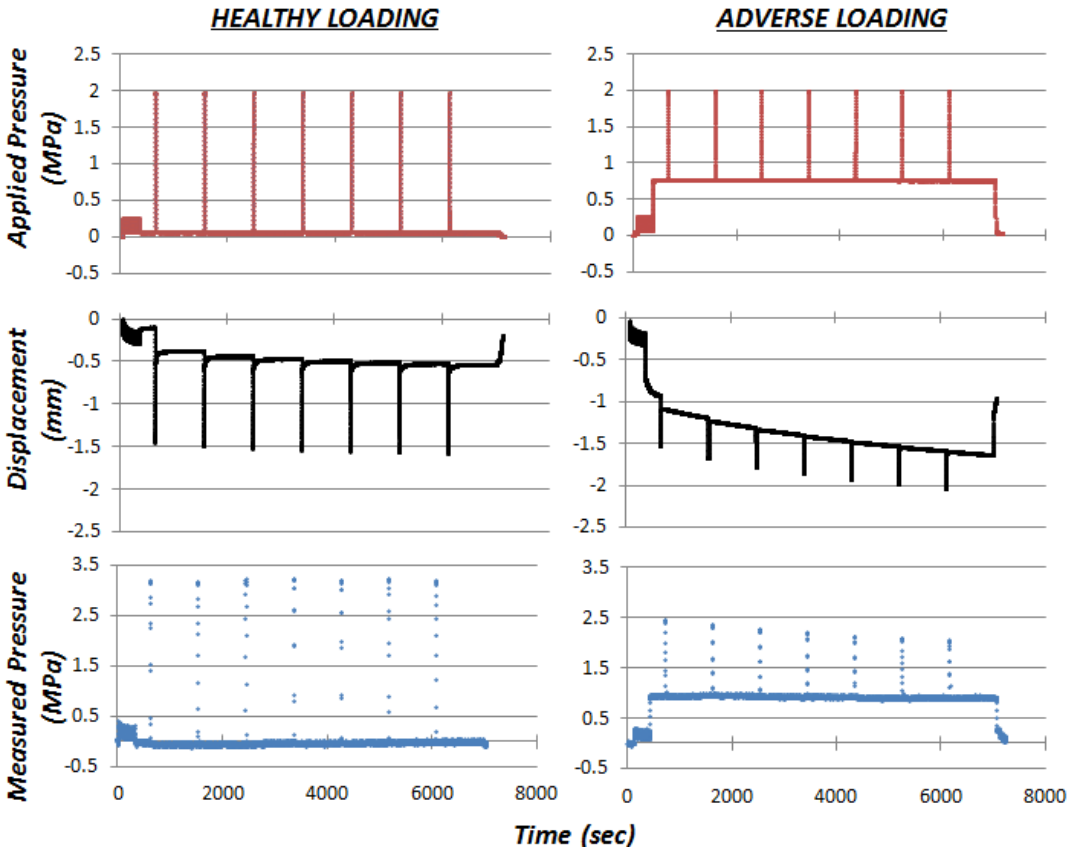

Figure 92: Overview of applied loading profiles with respective pressure and vertical displacement data. Loading profiles **(**Top Row), displacement data relative to the start of cyclic preconditioning (Middle Row), and pressure generated within the NP region for healthy and adverse conditions (Bottom Row).

heights recorded at a mid-vertebral position. Disc displacements were divided by preload disc height to obtain strain values, controlled for every motion segments' geometry. Motion segment disc heights were measured again after successful completion of experiments. Under healthy loading, L2L3 motion segments (n=3) lost an average 0.367±0.248mm and L4L5 motion segments (n=4) lost 0.844±0.589mm. For adverse loading, L2L3 motion segments (n=4) lost an average 0.800±1.051mm and L4L5 motion segments (n=3) lost 0.784±0.829mm. High standard deviations likely resulted from inconsistent timing and procedures between the conclusion of mechanical tests and radiograph imaging of post-load discs.

Motion segments exposed to healthy loading (n=9) exhibited compressive axial strains during challenge loading that were significantly smaller ($p<0.02$) than strains measured in adversely loaded discs (n=9) during equivalent challenges. The adverse group experienced continuously increasing strains during the 0.75MPa holds and averaged -44.0 ± 9.3 percent strain during 2MPa challenge loads. The healthy group averaged -30.0 ± 2.9 percent strain for the same 2MPa loads, and exhibited little to no additional strain during 0.05MPa holds.

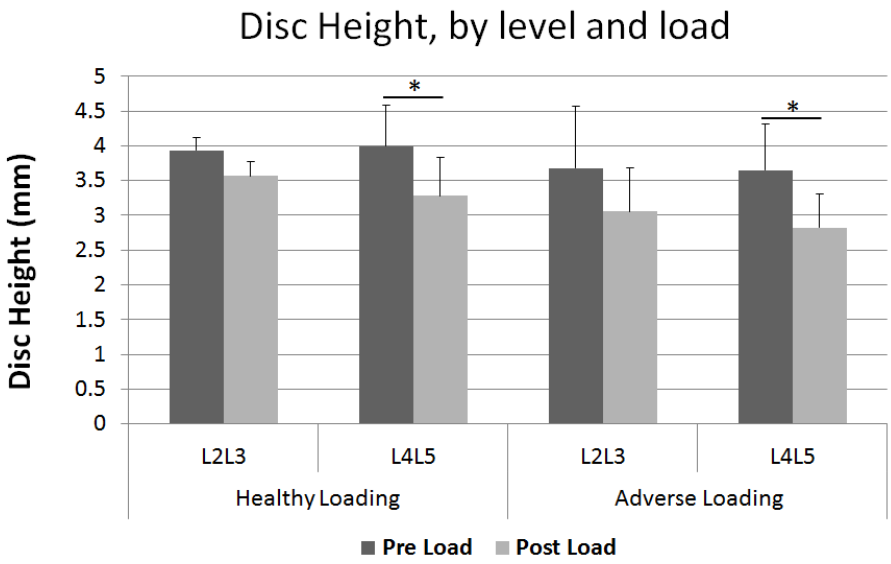

Figure 103: Pre- and Post-load disc heights by level and loading regimen. Average heights decreased for all motion segments following loading, Significant loss of disc heights were noted in L4L5 motion segments for both healthy and adverse loads ($p<0.05$).

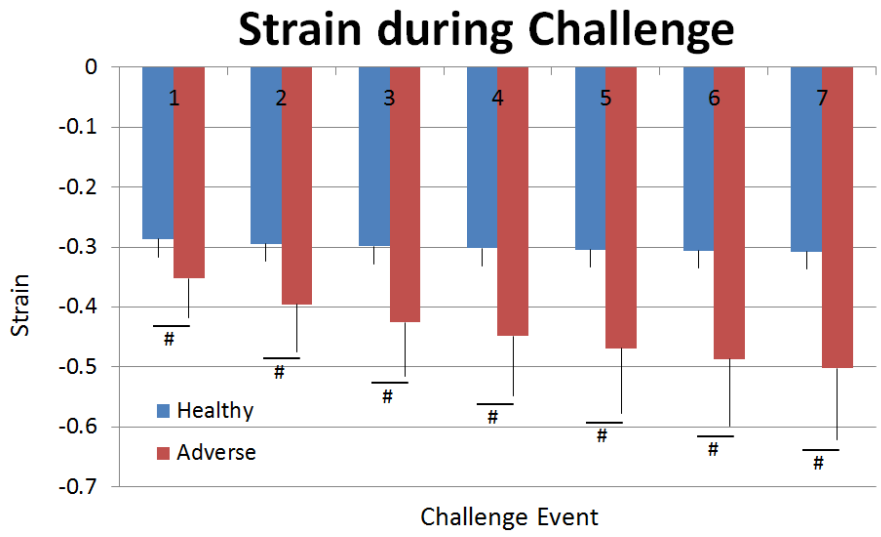

Figure 41: Measured strain at each transient challenge load. Maximum strains generated at each challenge remain approximately 30% of the disc height in the Healthy group (n=8) while strains in the Adverse group (n=9) continue to increase with each challenge. For all challenge loads, strain differences are significant ($p<0.05$) between healthy and adverse groups.

	Healthy Loading Group Disc Heights									
	Sh2 L2L3	Sh3 L4L5	Sh4 L2L3	Sh5 L4L5	Sh6 L2L3	Sh7 L4L5	Sh8 L4L5	Sh9 L4L5	Sh10 L4L5	Sh11 L2 L3
PRE-LOAD										
Anterior Corners	--	3.544	3.392	3.071	3.150	3.057	4.384	4.349	5.570	4.572
Mid Vertebral	--	4.549	4.636	5.239	4.955	3.791	2.556	3.324	4.502	2.877
AVERAGE		**4.046**	**4.014**	**4.155**	**4.053**	**3.424**	**3.470**	**3.837**	**5.036**	**3.724**
POST-LOAD										
Anterior Corners	--	--	3.362	2.340	2.763	--	3.144	4.284	4.155	3.789
Mid Vertebral	--	--	4.490	3.910	4.443	--	2.007	3.335	3.066	2.532
AVERAGE	--	--	**3.926**	**3.125**	**3.603**	**--**	**2.575**	**3.809**	**3.611**	**3.161**

	Adverse Loading Group Disc Heights										
	Sh2 L4L5	Sh3 L2L3	Sh4 L4L5	Sh4 L5L6	Sh5 L2L3	Sh6 L4L5	Sh7 L2L3	Sh8 L2L3	Sh9 L2L3	Sh10 L2L3	Sh11 L4L5
PRE-LOAD											
Anterior Corners	2.918	3.385	3.086	3.739	2.173	2.334	4.087	3.252	4.086	4.075	3.638
Mid Vertebral	3.964	4.514	4.867	5.529	3.065	3.858	4.784	2.101	5.443	3.165	2.550
AVERAGE	**3.441**	**3.950**	**3.976**	**4.634**	**2.619**	**3.096**	**4.436**	**2.676**	**4.765**	**3.620**	**3.094**
POST-LOAD											
Anterior Corners	--	--	--	2.361	1.901	1.624	2.372	3.331	2.772	4.589	3.843
Mid Vertebral	--	--	--	3.717	2.916	2.931	2.741	2.759	3.812	3.376	2.468
AVERAGE	--	--	--	**3.039**	**2.408**	**2.278**	**2.556**	**3.045**	**3.292**	**3.982**	**3.156**

Table 3: Pre- and Post-load disc heights. 'Anterior Corner' and 'Mid-Vertebral' values are representative means of three measurements from lateral radiographs**.** The average of both means was used as the disc height for strain calculations specific to each motion segment's geometry.

3.3.2 Physiological Modeling and Creep Parameters

Loading profiles were designed as two-hour creep loading experiments subjecting motion segments to either relatively high (0.75MPa) or neutral (0.05MPa) physiologic loads. Transient challenge loads were added solely to assess disc response during maximum compressive forces and identify differences between adverse and healthy loading groups. In the 15 minutes of constant applied force following each challenge, discs were expected to recover. Strain values from the last three seconds of each recovery phase were averaged and plotted in time to develop a quasi-creep curve for each specimen. The creep curves were fit to a fluid transfer model which assumes a pressure gradient across the vertebral endplate during creep loading. The model is comparable to three- and four-parameter viscoelastic solid (spring-and-dashpot) models, but includes parameters with greater physiological relevance (Cassidy et al., 1990). Model parameters D, G, k, and ε_o were acquired from curve fits of each motion segment's creep curve. Respectively, they represent strain dependent NP consolidation, time dependent tension in AF, endplate permeability, and initial strain.

$$\varepsilon(t) = \varepsilon_o + \left(\frac{\sigma_o - P_o}{D} - \frac{h_i G}{2kD^2}\right) \times \left[1 - \exp\left(-\frac{2kDt}{h_i}\right)\right] + \frac{G}{D}t \qquad \text{Equation 3.5}$$

Parameter D, representing the tendency of the NP to compress with strain, was significantly higher in the adverse group than the healthy group, independent of level. For L2L3, the average adverse group (n=5) value for D was 4.906 ± 2.212N/mm while the healthy group (n=4) average was 0.440 ± 0.238N/mm. For L4L5, the adverse group (n=4) averaged 3.338 ± 0.620N/mm while the healthy group (n=5) average was 0.598 ±

0.096N/mm. Level was insignificant: healthy L2L3's average D was not significantly different from healthy L4L5's average D. Similar insignificance was found between adverse L2L3 and adverse L4L5 D values.

Parameter G, representing the degree to which the AF was subjected to tensile loads over time, was found to be greater for the adverse group in both levels. For L2L3, the average adverse group (n=5) value for G was 6.520E-5 ± 1.364E-5 mm^2/sec while healthy group (n=4) average was 0.164E-5 ± 0.078E-5 mm^2/sec. For L4L5, the adverse group (n=4) averaged 6.893E-5 ± 0.611E-5 mm^2/sec while the healthy group (n=5) average was 0.223E-5 ± 0.164E-5 mm^2/sec. Level was insignificant: healthy L2L3's average G was not significantly different from healthy L4L5's average G. The same insignificance was found between the adverse L2L3 and adverse L4L5.

Parameter k, representing the resistance to fluid transfer across the vertebral endplate, was significantly higher in healthy L4L5 motion segments (n=5) than both the adverse L4L5 (n=4) and the adverse L2L3 (n=5) groups. There was no significance between healthy L2L3 and any of the other average k values due to the high standard deviation. To confirm, however, that the trends noted in the L4L5 group are applicable, all adverse k values were compared to all healthy k values and found a statistically significant difference ($p<0.001$). Adverse k values were approximately an order of magnitude lower than healthy k values.

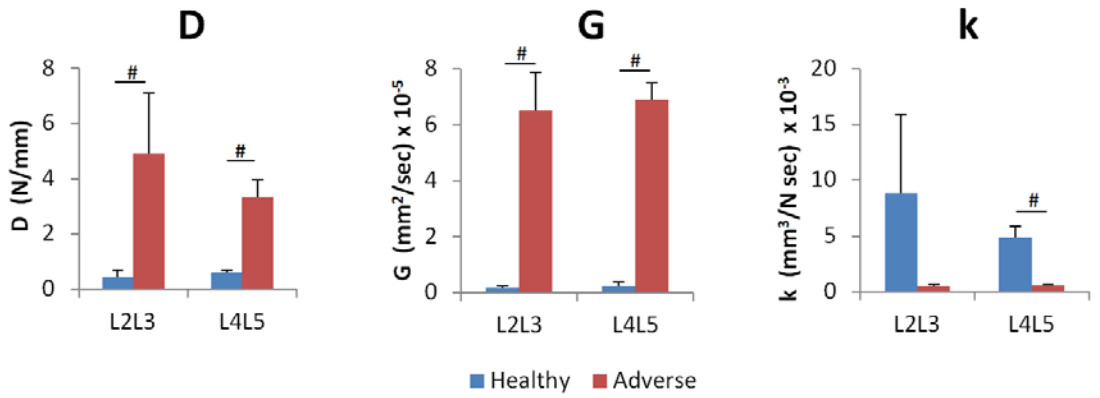

Figure 52: Creep Parameters. Curve fits of strain data were used to generate creep parameters for healthy and adversely loaded discs. Model outputs are shown separated by level. Statistical significance ($p<0.05$) is only indicated when appropriate within a level, though statistical significance does exist between levels for each parameter.

3.3.3 Adverse loading limits the ability to generate consistent pressure

Mechanical loading yielded two populations of NP pressures. The healthy group (n=8) maintained an average pressure of 0.061MPa during recovery loading at 0.05MPa, and demonstrated an ability to generate consistent maximum pressures during challenge loading: each challenge event generated pressures within 0.092 ± 0.082MPa of the pressure generated during the initial challenge. The adverse group (n=7) maintained an average pressure of 1.28MPa during recovery loading at 0.75MPa, and reduced the maximum NP pressure generated in each challenge, with an average loss of 0.311 ± 0.196 MPa in peak pressure between initial and final challenge events. Differences in pressure generation from initial to final challenge events were significant ($p<0.05$) between adverse and healthy groups.

Differences in load site (i.e. position of the rod relative to disc center of mass/axes of rotation) and each motion segment's unique tendency to pressurize resulted in a large range of observed NP pressures for the same loading profile. To correct for discs' ability to pressurize, pressures were normalized for each motion segment. Pressures measured

during each challenge event were divided by the maximum pressure observed during the initial challenge, to normalize the challenge pressures within each experiment. The normalized challenge pressures further exposed the trend that the healthy group maintained –or slightly increased– NP pressure generation in challenge loading for the entire experiment, while the adverse group was unable to generate consistent pressures during each challenge event. Changes in normalized maximum pressures were significant ($p<0.01$) between the healthy group's final challenge event (103.07 ± 2.89 percent initial pressure) and adverse group's final challenge event (90.08 ± 5.56 percent initial pressure).

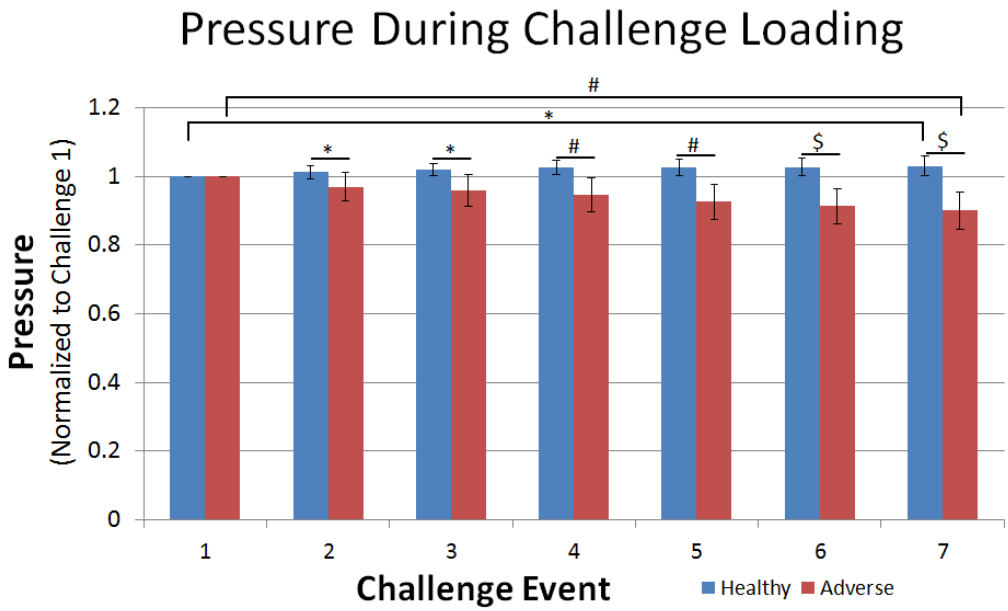

Figure 13: Measured NP pressure at each transient challenge load. Maximum pressures generated at each challenge load remained relatively stable, and in fact increased, within the Healthy group (n=8) while pressure generation decreased across challenge loads in the Adverse group (n=7). Statistical significance (p-value) markers: $0.05 \geq * > 0.01 \geq \# > 0.001 \geq \$$.

3.3.4 Intradiscal Shear and Intradiscal Pressure Relation

From the definition of octahedral shear stress, the principle stress values within the ovine disc were acquired as pressure readings and applied compressive force data.

Applied compressive force data from the MTS time history was divided by disc cross sectional area measurements recorded prior to testing to generate a value for compressive stress. Compressive stress was divided by the ratio of NP cross sectional area to whole disc cross sectional area to control for the NP's elevated resistance to compressive loading relative to the AF. O'Connor et al. (2007) reports a whole disc cross sectional area of 676mm^2 and an NP area of 267mm^2 for ovine L4L5 IVDs, suggesting a ratio of 0.39. Dividing the compressive stress by 0.39 yields the value for the vertical principle stress applied to the NP.

$$\sigma_1 = \sigma_{applied_{NP}} = \frac{\sigma_{compression}}{\left(\frac{267\ mm^2}{676\ mm^2}\right)} = \frac{\sigma_{compression}}{(0.39)} \qquad \text{Equation 3.6}$$

Again, it was expected that the principle stress applied to the NP was larger than the overall compressive load, since the NP represents only a small percentage of the disc's cross sectional area, but was responsible for resisting a large percentage of spinal compression.

Pressures perpendicular to the frontal plane were measured as described in previous sections detailing pressure measurement. Sensors were always inserted into the anterior face of the IVD. To compare pressures acting perpendicular to the frontal plane against pressures acting perpendicular to the sagittal plane, motion segments (n=2) underwent two short-term loading cycles each. For the first loading cycle, sensors were positioned to acquire pressures acting perpendicular to the frontal plane (anterior insertion). For the second loading cycle, sensors were positioned to acquire pressures

acting perpendicular to the sagittal plane (lateral insertion). Sensor position was confirmed using radiographs prior to each loading cycle.

Similar stress generation was measured in both directions for each motion segment. For each step in applied pressure, the average IDP was calculated in both directions. The ratio of sagittal:frontal IDP ranged between 0.85 and 1.76, reflecting mixed trends.

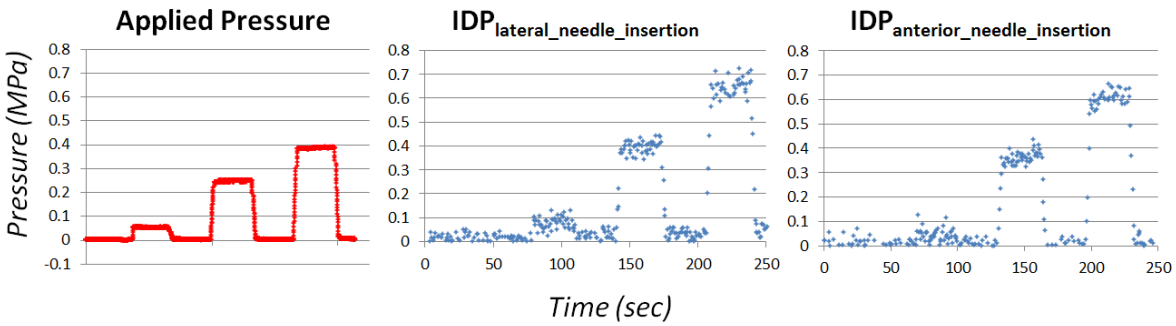

Figure 64: Force Profile and Observed Pressures for short-term loading cycles. Pressures perpendicular to sagittal (lateral needle insertion) and frontal planes (anterior needle insertion) were measured in subsequent experiments to compare directionality of stress in non-axisymmetric discs under compressive loading.

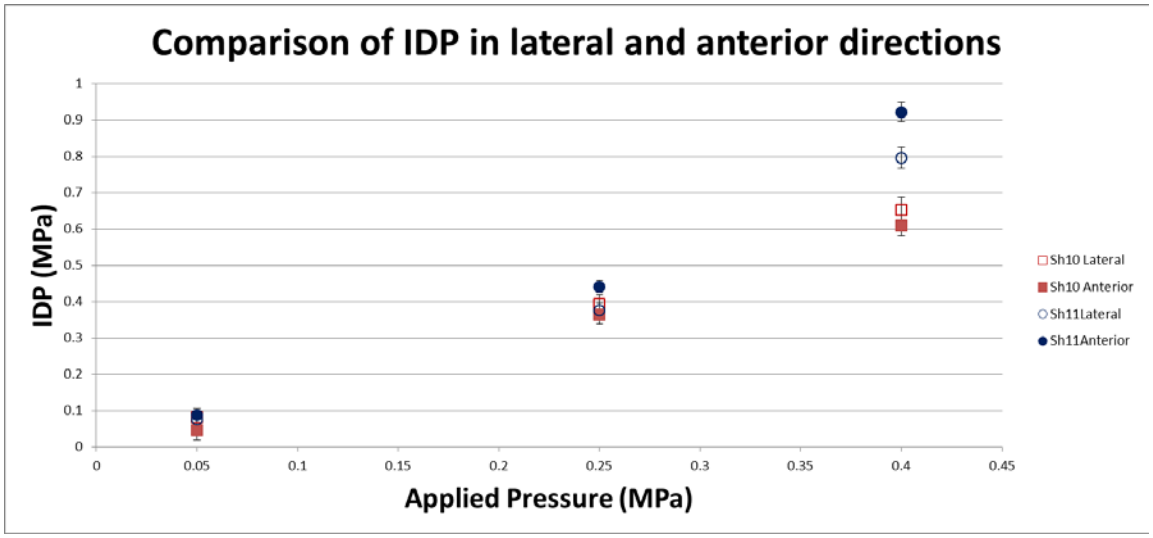

Figure 75: Observed Pressures in lateral and anterior directions. Different pressurization trends were noted between the two sheep. Sheep 10 generated higher pressures perpendicular to the sagittal plane, while pressures observed in Sheep 11 suggested greater pressure in the direction perpendicular to the frontal plane.

	SHEEP 10, L4L5				
	Lateral		*Anterior*		*Lateral/Anterior*
Applied Pressure	**Average**	**StDev**	**Average**	**StDev**	**Ratio**
0.05	0.081381	0.024884	0.046278	0.027297	1.76
0.25	0.394675	0.024341	0.364946	0.02507	1.08
0.4	0.653212	0.034883	0.610481	0.027479	1.07
	SHEEP 11, L2L3				
	Lateral		*Anterior*		*Lateral/Anterior*
Applied Pressure	**Average**	**StDev**	**Average**	**StDev**	**Ratio**
0.05	0.076885	0.021053	0.08899	0.011034	0.86
0.25	0.37713	0.019122	0.441806	0.01711	0.85
0.4	0.795716	0.029869	0.922613	0.027126	0.86

Table 4: Observed pressures (MPa) by direction of needle placement. Average of all ratios is 1.08.

For motion segments from one sheep, sagittal pressures tended to be larger than frontal pressures while in the other sheep, frontal pressures were larger, yet the averaged sagittal:frontal IDP ratio from all motion segments across all applied pressure steps was 1.08, and the sagittal:frontal IDP ratio was approximated as 1:1. Thus the remaining two principle stresses, σ_2 and σ_3 are assumed to be equivalent.

$$\sigma_2 = \sigma_{Pressure_X} \quad = \quad \sigma_3 = \sigma_{pressure_x} \times \left(\frac{Pressure_y}{Pressure_x}\right) \qquad \text{Equation 3.7}$$

Substitution and simplification of the three principle stress values (Eqn 3.6, Eqn 3.7) into the octahedral shear stress equation (Eqn 3.1) generates an estimate of intradiscal shear stress present within ovine lumbar NP.

$$\tau_{octahedral} = IDS = \frac{1}{3}\sqrt{\left(\frac{\sigma_{compression}}{(0.39)} - \sigma_{pressure}\right)^2 + \left(\sigma_{pressure} - \frac{\sigma_{compression}}{(0.39)}\right)^2} \qquad \text{Equation 3.8a}$$

Additional simplification yields:

$$\tau_{octahedral} = IDS = \frac{1}{3}\sqrt{2 \times \left(\frac{\sigma_{compression}}{(0.39)} - IDP\right)^2} \qquad \text{Equation 3.8b}$$

The final relation between intradiscal shear, vertical compressive stress, and intradiscal pressure:

$$IDS = \frac{\sqrt{2}}{3}\left(\frac{\sigma_{compression}}{(0.39)} - IDP\right) \qquad \text{Equation 3.8c}$$

Using the above equation, IDS was calculated at every challenge load. IDS averages for healthy and adverse groups were calculated to identify changes in response to loading condition with time. IDS values are presented with respect to IDP as the ratio IDS:IDP. This ratio demonstrates the trends of the shear stress while incorporating the effect of load on NP pressure. An increasing IDS:IDP trend was noted in the adverse group with the ratio increasing from 0.321 to 0.413, while a decreasing trend was noted in the healthy group, 0.336 to 0.312, between challenge 1 and challenge 7.

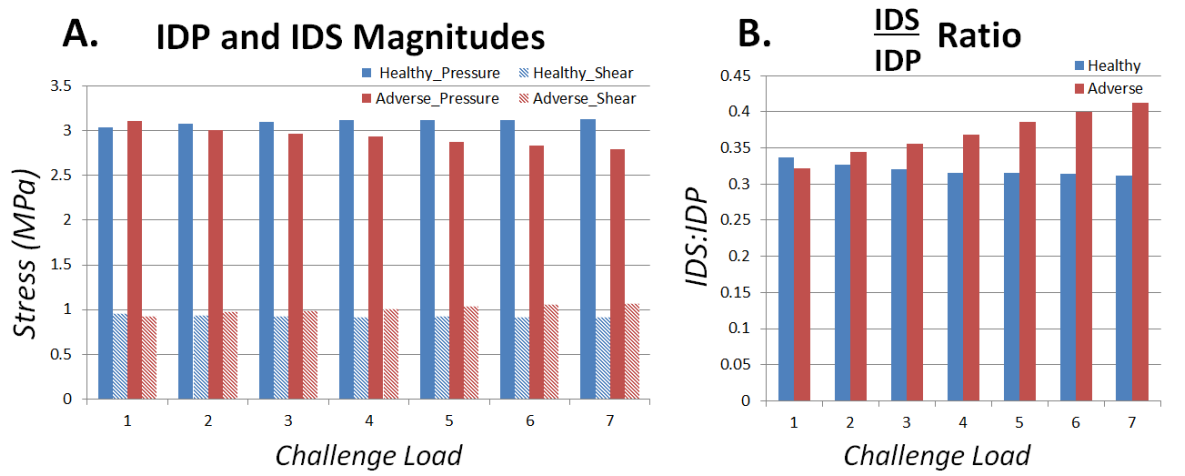

Figure 86: Intradiscal Shear and Intradiscal Pressure relation. Magnitudes (A) and ratios (B) for IDP and IDS demonstrate trends in the individual –and combined—values, for each challenge load. Note in (A) that adverse groups exhibit decreased pressure and increasing strain, while IDP and IDS values remain stable for the healthy group.

3.3.5 Assessment of disc bulge.

Preliminary bulge measurements were collected by orienting the laser triangulation device to a single location 30° laterally offset from the mid-sagittal plane. The device was set to observe the radial displacement of a visibly smooth section on the anterolateral AF surface at approximately one-third the total disc height, shown previously to exhibit the greatest degree of bulge under axial compression (Heuer et al., 2007; Pei et al., 2014). However, tissue compression during the experiment may have lowered the initial target position and readings may no longer represent radial bulge at a single location on the disc surface. Additionally, routine PBS sprays to maintain a hydrated disc surface resulted in bulge data that exhibited inconsistent readings. It was expected that increased bulging would occur during transient challenge loading, and while increased bulging was noted during periods of high load, so too were short-term increases of bulge noted with the same frequency that PBS hydrating spray was applied. Only when paired with time data, were transient increases in bulge due to challenge loading distinguishable from bulge increases resulting from PBS spray. The resulting data set was inherently noisy and demonstrated poor resolution between bulge measurements during challenge and recovery loading.

In a second attempt at collecting bulge data, a 1mm x 1mm square of reflective tape was attached to the disc surface with tissue adhesive, again at a position approximately 1/3 the disc height. The reflective tape was selected to provide three advantages: increase the amount of light reflected back to the laser device for improved signal, provide a consistent target point on the disc at which to aim the laser, and provide a surface slightly offset from the tissue surface so that PBS applied via a pipette would

not interfere with the reflecting surface. Still, measurements were noisy and resolution did not improve.

The most successful method used to acquire radial bulge measurements employed vertical scans across the full disc height at key moments in the loading profile throughout the experiment (i.e. before and after challenge loads, midway through each recovery stage). Results demonstrate that the outermost annulus was more complex than a single, smooth surface. Though the laser-reflecting surface was trimmed of all excess tissue, wiped with saline, and confirmed smooth by observation, non-uniformities along the disc surface were detected by the scanning apparatus. The disc's tendency to bulge radially under applied compressive loading was still apparent in some samples. Profiles of motion segments from the same sheep exposed to either adverse or healthy loading conditions are displayed.

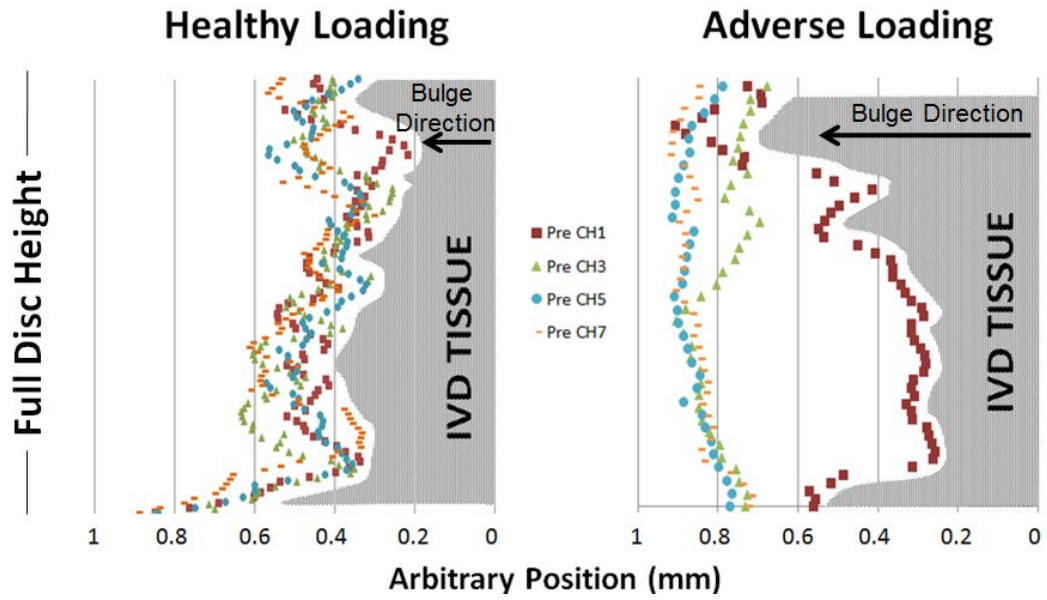

Figure 97: Disc profiles from radial bulge measurements. Scans were conducted before and after every challenge load but only scans recorded before challenge loads 1, 3, 5, and 7 are pictured. In both plots, profiles are drawn with respect to the IVD tissue (grey shading) and represent disc bulging from right to left. The vertical axis is representative of the disc height. Position (in mm) is not reported with respect to any specific zero point, but is used to measure changes in disc bulge between challenge events.

Average IVD bulge was computed from scans, by computing the mean position measuring across the full height of the disc. Pre- and post-challenge scans were compared within a challenge and across challenges to understand the effects of load magnitude and duration on disc bulge. In the healthy loading group, pre-load bulge values were 0.011±0.016 mm less than the post-load bulge measurements within the same challenge. The adverse loading group demonstrated pre-load bulge values that were 0.046±0.108 mm less than their respective post-load bulge counterparts.

While there is little difference in bulge before and after challenge loading there is noticeable change in bulge over the course of seven challenge loads, at least in the adverse loading case. Average bulge increased with increasing load duration (up to 0.439±0.040mm at the conclusion of challenge 7) for the adverse loading group but remained nearly unchanged in the healthy case (up to 0.057±0.098mm).

	AVERAGE BULGE DISPLACEMENT (mm)							
	Healthy				*Adverse*			
	Pre-Load	**Std. Dev**	**Post-Load**	**Std. Dev**	**Pre-Load**	**Std. Dev**	**Post-Load**	**Std. Dev**
Preconditioning	--	--	0	0.1038	--	--	0	0.1700
Challenge 1	0.0020	0.1057	0.0192	0.1028	0.0305	0.1914	0.3190	0.0608
Challenge 2	0.0088	0.0937	0.0412	0.1014	0.3414	0.0635	0.3405	0.0622
Challenge 3	0.0364	0.1103	0.0462	0.0979	0.3512	0.0609	0.3856	0.0534
Challenge 4	0.0342	0.1022	0.0208	0.1053	0.3988	0.0735	0.3932	0.0767
Challenge 5	0.0235	0.0947	0.0458	0.1015	0.4236	0.0434	0.4096	0.0409
Challenge 6	0.0245	0.0979	0.0394	0.0983	0.4281	0.0427	0.4331	0.0465
Challenge 7	0.0627	0.1150	0.0565	0.0977	0.4250	0.0496	0.4394	0.0395

Table 5: Bulge values (mm) reported as the change from bulge recorded at the end of preconditioning. Positive values indicate outward radial bulge. Average and standard deviations reflect only one motion segment for both the Healthy (n=1) and Adverse (n=1) groups.

3.4 Discussion

The NP region of IVDs uses its hydrated, gelatinous structure to transmit load between vertebrae by pressurizing as the disc was compressed. Different applied loads were expected to result in different tissue response, supporting the hypothesis that high compressive recovery loading inhibits biomechanical function of sheep lumbar motion segments as compared to low compressive recovery loading in ex vivo experiments. These different loading regimens were selected to demonstrate the loss of function and shift in biomechanics for different compressive loading environments.

Adverse loading increased strain and reduced the NP pressure during adverse loading. Similarly, creep parameters extrapolated from strain curves and shear:pressure ratios suggest different tissue responses to adverse and healthy loading conditions. The findings are presented herein as part of the larger body of IVD biomechanics research.

3.4.1 Adverse loading increases axial strain

In biological tissues, fluid plays a large part in regulating material deformation. This inherent viscoelasticity is well characterized in a variety of human tissues including the IVD, and dictates loading and recovery rates. Studies report non-degenerate ovine discs displacing 0.979±0.313mm, or 15 percent strain, after 5 minutes of creep testing at 1000N (Pei et al., 2014). Another experiment applied a 1000N compressive load to human lumbar levels L3-L4 and L4-L5 for 20 minutes and used magnetic resonance imaging to observe pre and post load displacements of 0.63mm, approximately five percent strain (O'Connell et al., 2011). Strains, reported as displacement divided by initial disc height, during final challenge loading measured 7.5 percent for healthy load

cases, but jumped to 42.2 percent in the adverse group. Excessive creep was noted throughout adverse recovery phases, enabling greater displacements during challenges.

Within the data set prepared for this thesis, adverse loading resulted in up to five times more strain than healthy loading. This is in agreement with data suggesting damaged and degenerate discs allow greater deflection than healthy equivalents. Human lumbar degenerate discs were identified and mechanically tested under 1000N creep loading and compared to healthy equivalents. Statistically larger displacements were recorded from degenerate discs than the healthy counterparts (O'Connell et al., 2011). The loss of NP structure (or loss of load-bearing function) may be the causal factor, as the study also cited that discs treated with a two gram nucleotomy –removal of 2g NP tissue– resulted in strains similar to untreated degenerate discs.

Tissues have been shown to recover fully when stored unloaded in a PBS bath chilled to 40°F, for 18 hours (Johannessen et al., 2004). Johannessen observed consistent disc stiffness and relaxation before and after two rounds of recovery for six lumbar sheep spines. Though the Johannessen study does not reflect in vivo conditions, diurnal cycling enables equivalent recovery in living tissues. In vivo pressure sensing in human lumbar IVDs demonstrates recovery of pressures during a 7 hour night's sleep, and recovery of disc height is expected to match the increasing fluidic pressures (Wilke et al., 1999). While the 0.05MPa recovery phase in the healthy loading profile can be observed as a recovery period, the time elapsed during 2MPa challenge loads and the 15 minute recovery load are not long enough to observe a traditional creep experiment followed by a full recovery phase (note that recovery of in vitro discs took 18hours of PBS submersion and in vivo recovery requires a seven hour supine position). Testing was

designed to observe creep response under 0.05MPa or 0.75MPa with transient challenges to measure resilience of IVDs under transient high loads, and thus it is difficult to assess alternate, long term relaxation and recovery.

3.4.2 Physiological Modeling and Creep Parameters

A number of models attempt to equate viscoelastic tissue deflection to load. Few are physiologically based, and even fewer represent three-dimensional changes. The equation proposed by Cassidy et al. includes parameters relatable to structural and physiological behavior, though the model is not perfect: it incorporates time- and strain-dependent pressure gradients across the vertebral endplates but assesses only one dimensional fluid flow from the disc (Cassidy et al., 1990). Intrinsic to the model are permeability (k), found to decrease in magnitude with increased applied stress, and strain- and time-dependent parameters (D and G, respectively), found to increase with increased stress (Hwang et al., 2012; Palmer et al., 2004). In these experiments, values for D and G increased with increasing stress, and k decreased.

Degeneration, however, may induce confounding effects. In a degenerative disk mouse model, increased loading demonstrated the typical increase in D and G and decreased k, but degenerate equivalents exhibited significantly lower D and slightly elevated k (Palmer et al., 2004). One explanation for such behaviors may be the effect of water concentration on the permeability of cartilage. The data collected for this thesis suggests permeability decreases with decreasing water content, explained by an intuitive consideration that with less water a lower pressure gradient exists. However, discs in the degenerative model may exhibit structural damage and disorganized aggrecan such that

inconsistencies in tissue hydration enable abnormal dispersion of water such that the one-dimensional water transport assumptions no longer reflect fluid behavior.

A complementary mechanism explaining reduced permeability in high load events may also relate to deformation of the extracellular matrix. As tissue is compressed, the extracellular matrix density increases and pore size is reduced. Compressed pore size limits fluid flow resulting in reduced permeability. Pore size is less affected during minor loads, since NP deflection is limited. This mechanism indicates that degenerative discs – those with a degrading, less dense extracellular matrix– will exhibit slightly elevated pore size and thus increased permeability, in agreement with Palmer et al. (2004).

The strain-dependent swelling pressure would increase if there was no fluid flow from a constant volume, and as such, parameter D should be expected to increase with increased load, as the tissue deflects to an increasing degree under increased load. However in the case of degenerate discs the statistically significant lower D value may result from the discs reduced ability to generate pressure under increasing strains. While strains –and the fluid pressures created by the strains– increase with increased load, degenerate models may not reflect an equivalent ability to preserve fluid pressure. Increased time-dependency, G, for elevated loading was expected so that shorter time was required to reach a steady state strain, a trend which was preserved for increasing loads as well as in the degenerate model study.

Creep experiments performed on mouse, rat, and mongrel canine discs have been assessed using the Cassidy fluid model (Palmer et al., 2004; Hwang et al., 2012; Cassidy et al., 1990). While magnitudes differ among all species previously studied, similar trends for D, G, and k are preserved. The values reported herein may provide guidance for ovine

IVD fluid flow experiments and help to validate further applicability of both healthy and degenerate ovine disc experimentation to human equivalents.

3.4.3 Adverse loading limits the ability to generate consistent pressure

Intradiscal pressure measurements have developed into a standard method for observing IVD behavior, and are assessed as a corollary to the fluid within the NP. In vitro and in vivo studies have demonstrated the diurnal pressurization of tissues as well as IVD response to loading events, with a broad range of sensors (Wilke et al., 1999; Claus et al., 2008; Adams et al., 1996; Vergroesen et al., 2014). For this study, discs were subjected to one of two compressive creep loads, each with transient challenge loads. The 0.05 and 0.75MPa recovery loads, were intended to replicate in vivo IDPs recorded during prone resting and standard load activities (Sato et al., 1999; Wilke et al., 1999; Claus et al., 2008), and transient 2MPa exertions were meant to replicate high force challenges such as heavy lifting or other strenuous activity.

Resultant NP pressures observed for all phases of loading were reportedly greater than the target applied pressure. In experiments completed immediately after adverse or healthy loading procedures, discs demonstrated pressures approximately 1.73±0.39 times greater than the target applied pressure, with no distinct difference between healthy and adverse loading groups. This elevated observed pressure can be linked to the discs biphasic nature. As was described in the development of the IDS equation, and supported by the assessment of creep parameters (notably D, strain-dependence), compressive force transmission in not equivalent between NP and AF regions. The fluidic nature of the NP resists compression while the fibrous AF resists tensile loads from NP circumferential expansion under compressive loads. According to this commonly accepted mechanism,

and the NP's cross section relative to the full disc area, the NP can expect to experience higher pressures than the applied loading pressure.

Water distribution within the disc was considered a key contributor to the relative abilities of discs to pressurize during loading events. During transient challenges, the disc was compressed for a short time, causing deflection of the superior vertebrae and momentarily reducing the total disc height. Assuming fluidic incompressibility of the NP, volume constraints required the NP expand circumferentially into the AF to maintain its initial volume. At this point, two mechanisms acted simultaneously to balance the high pressures within the NP. The first was the tension afforded by the AF to maintain NP position and prevent NP exclusion or herniation. Bulge scans recorded before and after challenge loads were insufficient in capturing the short-term effects of high loading on AF bulge. However, preliminary experiments that observed a single position on the outer AF demonstrated distinct bulging during challenge loads. Simultaneously, the pressure gradient across the vertebral endplate enabled a percentage of the pressurized NP fluid to permeate the endplate. As load was removed from the motion segment viscoelastic time-dependent recovery returned NP shape, released AF tension, and enabled fluid return to NP. Curiously, higher endplate permeabilities (k) in the healthy loading group, suggest greater fluid expulsion from the NP. However only pressure measurements of adverse group's challenge load revealed a continual reduction in maximum pressure generation. Challenge loads may be equally effective at expelling water from the NP in both adverse and healthy groups, but the enhanced permeability and smaller recovery-phase pressure gradient in the healthy group may enable more efficient fluid return following challenge loading. Limited return of fluid to adverse loaded motion segments may explain why

greater strains and lower pressures are noted over the time course of the loading profile. An alternate, yet complementary mechanism relating high endplate permeability to consistent NP pressure recovery and limited compressive strain refers back to the density of the extracellular matrix. High loading increases strain which compresses matrix materials into each other, increasing matrix density, reducing permeability, influencing fluid pressure in the NP.

Relative NP pressure magnitudes within each motion segment were often used to establish trends between adverse and healthy loading. Absolute pressure measurements, though meaningful, raised more questions than they answered. Experimental design necessitated pairing each motion segment with a second motion segment harvested from the same sheep to control for genetic, diet, age, activity and other factors. Pressure generation was expected to be consistent at least within each sheep, with adversely loaded motion segments unable to generate the same IDP as their healthy counterparts during the same 2MPa challenge loads. However, for about half of the sheep in which both motion segments were successfully tested, pressures during challenge load 1 were higher in adverse than healthy groups. Inconsistencies in pressure generation, even within motion segments harvested from the same sheep limited the statistical significance of absolute pressure data, however, the trends in pressure loss between healthy and adverse groups' challenge loads were still present in the absolute pressure data. During the final challenge load, adverse groups average IDP was 2.795±0.521MPa compared to the 3.127±0.502MPa (healthy). The adverse group lost an average of 0.311MPa between first and last challenge while the healthy group's average IDP increased 0.092MPa between the first and last challenge load.

3.4.4 Intradiscal Shear and Intradiscal Pressure Relation

Shear is known to affect biomechanical regulation of cells in a variety of tissues, within all phases of the cell cycle. Differentiation pathways and post-differentiation phenotype have been shown to be shear-responsive. In bone growth and remodeling, high shear stress deforms precursor cells initiating formation of fibrous connective tissues; lower shear levels stimulate chondrocytes; and the lowest levels of shear enable ossification (Lacroix et al., 2002). Within NP cells, mechanoregulation has been linked to localized shear stresses (Wang et al., 2011). Cellular bioreactors report phenotypic changes under shear in the Pa to kPa range, and considering the lack of protective ECM and other experimental limitations in place to protect cell overstress rarely are experiments run –or reported—detailing cell death at elevated shear loads. Similarly, calculations from an in vitro rat study report maximum experienced shear stresses to be less than 350kPa (Hwang et al., 2012).

The focus of this thesis, however, was not to assess the effect of shear on cells and tissue but to quantify shear stresses present within the NP during in vitro loading events and discuss shear stress in the context of disc health. Theoretical calculation of shear stress in ovine discs yielded stresses on the order of 1MPa. Differences between the MPa-range values observed in this testing and the Pa and kPa stresses previously reported in bioreactor and small mammal studies may be due to tissue size and structure as well as the magnitude of normal physiologic load. While loads were controlled to reflect tissue size and geometry, the magnitudes of the applied forces remained larger than forces applied to the same cells and tissues in equivalent experiments. Since loading was intended to reflect physiological values, and shear stresses were calculated from tissue

responses to physiologic loads, larger mammals may be expected to endure increased magnitudes of intradiscal shear.

High magnitude shear environments are often used to break up cells and membranes in a variety of experimental procedures. In the extreme case, mechanical disruption of NP cells or ECM may result in high shear environments, triggering apoptosis or rupturing cell membranes and releasing cytoplasmic contents. Limited vascularization and solute diffusion may further damage surviving cells and inhibiting natural function. Though elevated shear stress magnitudes should be considered in NP cell processes, the relationship between NP pressure and IDS may indicate additional avenues for damage.

An alternate metric to assess potential damage or hazardous loading of the disc is the ratio IDS:IDP. An increasing ratio indicates increased radial migration of the NP, resulting in lower NP pressure generation and increased compression loads transmitted within the AF (Hwang et al., 2012). The fibrous character of the AF is intended to resist tensile loads induced during NP pressurization, not compressive loads between vertebrae. Atypical load sharing may contribute to damage –or even degeneration– within the IVD. The average IDS:IDP values from both adverse and healthy groups did not exceed 0.45, though ratios as high as 1:1 have been reported for adverse preloading experiments (Hwang et al., 2012). While IDS:IDP values did not alone reach dangerous levels, the trends in the data support an alternate damage mechanism. IDP was shown to decrease with each challenge load, and simultaneously, calculated IDS increased. This trend is evidence that innocuous, yet elevated loading during rest and recovery may, with time, induce damage due to accumulating effects.

3.4.5 Assessment of disc bulge.

Disc bulge measurements have been used in many studies as a non-contact method to observe IVD response to a variety of compressive, torsional, and bending loads. As early as the 1980's, human lumbar motion segments have been subjected to various loading types and bulge measurements, but the wide range of loading application and varied measurement procedures has produced a variety of reported bulges. Axial compression to 800N in human lumbar motion segments resulted in bulge up to 2.7mm in one study while similar loading resulted in an average bulge less than 1mm in another (Reuber et al., 1982; Stokes et al., 1988).

Recently, extensive scans or observation of multiple positions along the full disc height to obtain a more consistent understanding of disc bulge. A 500N compressive creep load was applied to L4-L5 human motion segments with 360° scans taken before load application and 15 minutes after load application. Greatest bulge, approximately 1mm, was observed in the anterolateral and anterior regions of the disc, while posterior and posterolateral bulge ranged between 0.25 and 0.5mm (Heuer et al., 2007). Motion capture of markers distributed across the disc have also enabled bulge assessment. Alternatively, alignment of markers in a vertical line on the posterolateral surface enables examination of bulge within different horizontal planes. Five markers were positioned vertically on the posterolateral surface of fifteen lumbar and thoracic ovine motion segments subjected to 200N, 600N or 1000N axial creep loads after a preconditioning cycle. While unexpected trends were present for different loads, maximum deformations (~0.4-0.5mm) were reported for markers inferior to the midpoint of the disc's height (Pei et al., 2014). Attempts to collect bulge data for this thesis assumed the greatest bulge

would occur at a posterolateral position, and vertical scans were used to assess bulge across the full disc height. Maximum deflections of approximately 0.2mm during the healthy loading events (0.05MPa, ~140N), and 0.6mm after adverse loading (0.75MPa, ~400N) were recorded. Profiles were excessively noisy, though displacements are within range of reported data. Additionally, the expectedly smooth contour of the outer annulus was non-uniform, rendering interpretation difficult.

Disc bulge has been reported to be time dependent under creep loading, and suggested to correlate with both intradiscal pressure and axial compression (Heuer et al., 2007; Pei et al., 2014). While bulge results align with time dependent and axial compression correlations, the continuously increasing bulge values are not complemented by increasing NP pressures. While bulge profiles displace further and further following each challenge load, sensor outputs indicate NP pressure was maintained. This disconnect led to additional review of the paper citing disc bulge as a direct indicator of internal hydrostatic pressure (Pei et al., 2014). The authors' interpretation of literature, namely, published work describing hydrogel constructs, may have been flawed. Hydrogels acting as a uniform material may be expected to bulge during unconfined compression with a predictable value of radial bulge equivalent to the applied load according to Poisson effect. While increased NP pressure should correlate to bulge, the direct relation between bulge and internal hydrostatic pressure is likely lost due to the multi-phasic nature of IVD tissues and complex mechanism for load bearing and NP pressurization.

A number of improvements could be made to advance radial bulge measurements. The current gold standard is a circumferential scan of the disc which simultaneously observes the full disc height. Full, 360°, circumferential scans, however, require removal

of vertebral posterior features thought to play a role in force transmission and stabilization between vertebrae. A scan of approximately 270° centered about the anterior face of the disc, sweeping laterally ±135° may be the best method to acquire sufficient surface bulge data while preserving the functional components of each motion segment. Two-dimensional laser displacement devices exist on the market for a wide range of applications and could be used for static observation at a single angular position or incorporated into a scanning mechanism for circumferential sweeps to observe bulge at all angular positions. The largest characteristic that the bulge data set lacked was distinct position values for the bulge measurements. While consistent positons were used as maximum and minimum scan heights, there was no record of the vertical position for each bulge data point. Distinctions between vertebral bodies and disc profiles were approximated using the scan profile and recorded notes from the day of testing.

3.5 Significance

Load history largely influences fluid-related biomechanics of the IVD. Indirect fluid measurements (NP pressure, axial strain, and radial bulge) indicate higher NP pressures –and elevated transport rates– during high loading. Endplate permeability was shown to be load-dependent: high compressive loads consolidate the NP, increasing ECM density, reducing porosity, and limiting fluid recovery despite favorable pressure gradients between vertebrae and IVD. High IVD loading was shown to limit fluid recovery and does not facilitate consistent pressure generation during subsequent high loading events. Reduced IDP generation during adverse loading was correlated to elevated IDS which has been shown to indicate damage within IVDs.

Chapter 4: Conclusions

4.1 Summary

Sheep lumbar motion segments are validated and often used to assess IVD biomechanical properties translatable to the human lumbar spine (Wilke et al., 1997; Smit et al., 2002). The enclosed findings provide additional understanding of the dynamics of short-term loading and recovery in ovine intervertebral discs. Further interpretation may provide physiological insight into load-induced biomechanical changes to guide clinical treatment of IVD degeneration and loss of function in human patients. Key findings from this study include:

- **High IVD loading during recovery phases inhibits NP pressure generation during challenge loads.** For challenge loads 2-7, the adverse loading group demonstrated an inability to pressurize to the same level as the first challenge. Meanwhile, the healthy loading group consistently met or exceeded the initial challenge pressure during all subsequent challenges.
- **Reduced IDP generation indicates elevated IDS.** Adverse loading tests demonstrated linearly increasing IDS:IDP ratios while healthy controls demonstrated decreasing trends. High loading reduced pressure generation, but increased shear during each subsequent challenge event.
- **Endplate permeability is load-dependent**. Permeability values (k) and displacement trends indicate fluid return during recovery phases was enhanced for heathy loading groups, and limited for adverse loading groups. Permeability

affects more than just fluid recovery, as nutrient transfer within the avascular IVD is fluid flow dependent.

Each of these points addresses the hypothesis that high loading limits fluid recovery and alters IVD biomechanics. Clinical treatments for lower back pain and degenerative disc disease must address the presence –and distribution– of fluid within the NP and surrounding tissues.

Forward thinking, proactive approaches to preserve disc health require novel procedures to enhance fluid return to NP tissue, but should also acknowledge the effect of lifestyle on disc recovery. Body weight, occupational demands, daily activity levels, sleeping habits and a number of other everyday choices can play a role in disc loading and more importantly disc unloading and recovery. We demonstrate that relatively high recovery loads –associated with obesity, a manual labor work environment, or regular sleep deprivation (limited time spend laying in a horizontal position suggests more time spent with an erect spine) – limits disc height recovery, impairs the ability to generate consistent NP pressures, increases IDS, and restricts nutrient exchange due to reduced endplate permeability. Lifestyles which limit the time IVDs experience neutral, recovery-promoting loads, increase the potential for damaged, and even degenerate, discs.

4.2 Future directions

This work was completed as part of a multipart study aiming to identify postural interventions effective at reversing critical loss of biomechanical function. Conclusions

from this phase of the study inform the time and load history dependencies associated with loss of IVD function. The next step will be to assess physical therapy-type motions –flexion, extension, torsion, traction or some combination– which mitigate or even reverse the effects of sustained, adverse loading. Regular completion of such interventional, non-invasive practices may improve long-term disc health by enabling regular recovery of biomechanical function.

To better assess biomechanical function, improvements to the bulge measurement system are essential. Current methods do not enable consistent, repeatable measurement of radial bulge. Laser displacement systems which enable two dimensional observation could be incorporated onto a rotational arm which moves circumferentially about the disc. Simultaneous recording of bulge values and circumferential angle and vertical position enable three dimensional mapping of the outer AF surface before, during, and after loading and any postural interventions.

Redesign of the test fixtures is required before physical therapy-type movements can be attempted on motion segments loaded in the MTS. The current inferior potting fixture stands atop four rollers which enable two degrees of translational freedom and one degree of rotational freedom and was designed to support purely compressive loading. If torsional or traction forces were to be applied to the current test set-up, the specimen would lose contact with the lower platen in the MTS machine.

Additional work can be done to further elucidate the effects of load history on disc properties. Cyclic loading, stress relaxation, and other creep loading profiles can be designed –or combined– to better isolate specific tissue response. High load conditions may expectably lead to loss of function, but compounding effects of moderate or even

low innocuous loads may help or hurt IVD mechanics depending upon prior loading conditions.

Modeling has been used in conjunction with, and as an alternative to, in vitro testing to characterize IVD biomechanics. The enclosed work provides data to inform more complex models, yet computer models may also improve the assumptions and validate conclusions made within this study. A model of the disc, including appropriate dimensioning and mechanical properties for the AF and NP regions may enable improved predictions of NP stress during development of the intradiscal shear equation. To date, a ratio of cross sectional areas was used to predict the stress state in the NP, though models of the full disc may more effectively enable NP stress state predictions. The relationship between total applied stress and the stresses experienced within distinct regions of the IVD will inform IDS calculations and further develop an understanding of disc loading environments and mechanisms.

Finally, meaningful findings and theories must be translated to the clinic. Oftentimes bench-top and other laboratory results are difficult to incorporate safely into practice, but this project, and others which will inevitably follow it, must aim to further the knowledge of disc biomechanics in a way that can simultaneously maintain disc function, preserve disc health, and improve patient care. This work demonstrated that different recovery loads influence disc behavior. Specifically, reduced –or removed– loads enabled disc recovery after periods of exertion. Proper disc recovery allowed return of disc height and consistent pressurization in our testing which may translate to improved disc health and extended disc effectiveness later in life. Recovery loading may be related to a variety of lifestyle factors, including body weight, daily activity levels,

occupation, and sleeping habits. Elevated baseline resting loads associated with obesity, heavy manual labor occupations, or regular sleep deprivation (limited time spend laying in a horizontal position) may limit IVD recovery, but there may be ways to improve IVD recovery through lifestyle choices and physical therapy type movements. Proactive and restorative activities alike should not be developed by researchers and lab technicians only to be lost in translation to the clinical environment. Disc health and function can only be preserved when research findings are transferable to physicians and patients alike, such that IVD research progress directly advances patient care.

Appendix

A.1 Position Data for Displacement Analysis

Position data for pre-challenge ('Pre'), challenge ('Max'), and post-challenge ('Post') time points for healthy and adverse loading conditions, as acquired from the MTS machine. There is no significance to an absolute zero position; instead, the post-preconditioning position is representative of a starting position for which super-hydration effects have been eliminated. All position data is reported in millimeters. Position data is not reported for tests that were stopped due to potting failure or other cases yielding an incomplete data set. Data is not reported for Sheep 1.

	Sheep 2											
	Healthy						**Adverse**					
	Pre	*Stdev*	*Max*	*Stdev*	*Post*	*Stdev*	*Pre*	*Stdev*	*Max*	*Stdev*	*Post*	*Stdev*
Precond.	--	--	--	--	-19.0573	0.0013	--	--	--	--	-8.4205	0.0008
Ch1	-18.7767	0.0011	-20.1086	0.0145	-19.0129	0.0056	-9.2136	0.0004	-9.8948	0.0122	-9.3794	0.0037
Ch2	-18.9329	0.0009	-20.1379	0.0125	-19.0629	0.0074	-9.5455	0.0004	-10.1241	0.0088	-9.6140	0.0031
Ch3	-18.9832	0.0008	-20.1616	0.0099	-19.0741	0.0029	-9.7195	0.0006	-10.2631	0.0071	-9.7660	0.0033
Ch4	-19.0120	0.0013	-20.1744	0.0114	-19.1120	0.0059	-9.8443	0.0005	-10.3747	0.0060	-9.8839	0.0029
Ch5	-19.0304	0.0009	-20.1918	0.0073	-19.1157	0.0033	-9.9458	0.0006	-10.4705	0.0056	-9.9835	0.0029
Ch6	-19.0460	0.0009	-20.2001	0.0078	-19.1357	0.0048	-10.0355	0.0005	-10.5551	0.0055	-10.0676	0.0028
Ch7	-19.0600	0.0010	-20.2055	0.0073	-19.1447	0.0036	-10.1147	0.0007	-10.6293	0.0055	-10.1462	0.0029

	Sheep 3											
	Healthy						**Adverse**					
	Pre	*Stdev*	*Max*	*Stdev*	*Post*	*Stdev*	*Pre*	*Stdev*	*Max*	*Stdev*	*Post*	*Stdev*
Precond.	--	--	--	--	-4.0773	0.0031	--	--	--	--	-5.3187	0.0044
Ch1	-3.9240	0.0010	-5.0649	0.0131	-4.1222	0.0036	-6.1243	0.0007	-6.6600	0.0118	-6.2526	0.0031
Ch2	-4.0245	0.0010	-5.0944	0.0092	-4.1838	0.0107	-6.4858	0.0008	-6.9540	0.0067	-6.5530	0.0020
Ch3	-4.0633	0.0011	-5.1082	0.0084	-4.2051	0.0093	-6.7018	0.0004	-7.1485	0.0061	-6.7552	0.0025
Ch4	-4.0836	0.0010	-5.1202	0.0098	-4.2255	0.0094	-6.8654	0.0006	-7.3075	0.0054	-6.9087	0.0015
Ch5	-4.1045	0.0010	-5.1299	0.0092	-4.2474	0.0112	-7.0063	0.0005	-7.4443	0.0044	-7.0522	0.0021
Ch6	-4.1226	0.0011	-5.1354	0.0110	-4.2376	0.0063	-7.1301	0.0005	-7.5612	0.0046	-7.1669	0.0017
Ch7	-4.1275	0.0014	-5.1422	0.0100	-4.2620	0.0085	-7.2347	0.0005	-7.6614	0.0041	-7.2738	0.0026

	Sheep 4											
	Healthy						**Adverse**					
	Pre	*Stdev*	*Max*	*Stdev*	*Post*	*Stdev*	*Pre*	*Stdev*	*Max*	*Stdev*	*Post*	*Stdev*
Precond.	--	--	--	--	-1.1643	0.0029	--	--	--	--	-3.2545	0.0038
Ch1	-1.0118	0.0009	-2.1955	0.0170	-1.2117	0.0050	-4.2436	0.0015	-4.9360	0.0134	-4.4646	0.0042
Ch2	-1.1055	0.0010	-2.2346	0.0125	-1.2552	0.0066	-4.6835	0.0016	-5.2381	0.0131	-4.7650	0.0029
Ch3	-1.1436	0.0008	-2.2489	0.0156	-1.2688	0.0047	-4.9121	0.0017	-5.4511	0.0087	-4.9769	0.0040
Ch4	-1.1685	0.0009	-2.2717	0.0123	-1.2797	0.0046	-5.0864	0.0018	-5.6106	0.0100	-5.1419	0.0022
Ch5	-1.1863	0.0014	-2.2804	0.0153	-1.3118	0.0036	-5.2296	0.0016	-5.7457	0.0082	-5.2858	0.0033
Ch6	-1.2039	0.0010	-2.2996	0.0082	-1.3348	0.0099	-5.3535	0.0022	-5.8661	0.0099	-5.4051	0.0025
Ch7	-1.2163	0.0008	-2.3035	0.0123	-1.3401	0.0062	-5.4648	0.0016	-5.9749	0.0081	-5.5160	0.0032

	Sheep 5											
	Healthy						**Adverse**					
	Pre	*Stdev*	*Max*	*Stdev*	*Post*	*Stdev*	*Pre*	*Stdev*	*Max*	*Stdev*	*Post*	*Stdev*
Precond.	--	--	--	--	-7.1872	0.0030	--	--	--	--	--	--
Ch1	-7.0297	0.0014	-8.3729	0.0289	-7.3225	0.0128	--	--	--	--	--	--
Ch2	-7.1822	0.0008	-8.4301	0.0276	-7.3416	0.0048	--	--	--	--	--	--
Ch3	-7.2362	0.0007	-8.4672	0.0236	-7.3924	0.0048	--	--	--	--	--	--
Ch4	-7.2733	0.0007	-8.4994	0.0144	-7.4323	0.0117	--	--	--	--	--	--
Ch5	-7.2965	0.0010	-8.5127	0.0210	-7.4502	0.0089	--	--	--	--	--	--
Ch6	-7.3135	0.0011	-8.5266	0.0218	-7.4706	0.0085	--	--	--	--	--	--
Ch7	-7.3323	0.0008	-8.5342	0.0233	-7.4703	0.0058	--	--	--	--	--	--

	Sheep 6											
	Healthy						**Adverse**					
	Pre	*Stdev*	*Max*	*Stdev*	*Post*	*Stdev*	*Pre*	*Stdev*	*Max*	*Stdev*	*Post*	*Stdev*
Precond.	--	--	--	--	-0.7346	0.0020	--	--	--	--	-6.9588	0.0018
Ch1	-0.6087	0.0007	-1.9291	0.0185	-0.9948	0.0108	-7.6411	0.0005	-8.2269	0.0100	-7.7978	0.0010
Ch2	-0.8867	0.0006	-1.9789	0.0136	-1.0424	0.0058	-7.9017	0.0003	-8.3792	0.0054	-7.9492	0.0012
Ch3	-0.9450	0.0006	-2.0119	0.0108	-1.0872	0.0084	-8.0176	0.0007	-8.4813	0.0032	-8.0517	0.0009
Ch4	-0.9768	0.0009	-2.0317	0.0101	-1.1045	0.0057	-8.1047	0.0005	-8.5604	0.0037	-8.1373	0.0018
Ch5	-1.0022	0.0007	-2.0474	0.0096	-1.1111	0.0045	-8.1792	0.0005	-8.6256	0.0045	-8.2064	0.0019
Ch6	-1.0175	0.0010	-2.0574	0.0121	-1.1240	0.0040	-8.2407	0.0008	-8.6862	0.0047	-8.2688	0.0020
Ch7	-1.0302	0.0007	-2.0722	0.0100	-1.1157	0.0022	-8.2948	0.0011	-8.7408	0.0040	-8.3208	0.0013

	Sheep 7											
	Healthy						**Adverse**					
	Pre	*Stdev*	*Max*	*Stdev*	*Post*	*Stdev*	*Pre*	*Stdev*	*Max*	*Stdev*	*Post*	*Stdev*
Precond.	--	--	--	--	--	--	--	--	--	--	-5.0282	0.0035
Ch1	--	--	--	--	--	--	-5.8456	0.0008	-6.4935	0.0127	-6.0607	0.0020
Ch2	--	--	--	--	--	--	-6.2403	0.0009	-6.7461	0.0084	-6.3069	0.0017
Ch3	--	--	--	--	--	--	-6.4289	0.0014	-6.9226	0.0056	-6.4802	0.0022
Ch4	--	--	--	--	--	--	-6.5754	0.0010	-7.0576	0.0074	-6.6175	0.0020
Ch5	--	--	--	--	--	--	-6.6987	0.0009	-7.1709	0.0057	-6.7351	0.0019
Ch6	--	--	--	--	--	--	-6.8028	0.0012	-7.2704	0.0051	-6.8398	0.0029
Ch7	--	--	--	--	--	--	-6.8913	0.0013	-7.3537	0.0034	-6.9273	0.0034

	Sheep 8											
	Healthy						**Adverse**					
	Pre	*Stdev*	*Max*	*Stdev*	*Post*	*Stdev*	*Pre*	*Stdev*	*Max*	*Stdev*	*Post*	*Stdev*
Precond.	--	--	--	--	-0.3081	0.0020	--	--	--	--	-0.3213	0.0021
Ch1	-2.9032	0.0007	-1.4348	0.0041	-0.2004	0.0025	-0.8263	0.0052	-1.4170	0.0038	-0.9432	0.0019
Ch2	-2.9772	0.0007	-1.4498	0.0034	-0.2113	0.0029	-0.9806	0.0006	-1.4750	0.0021	-1.0083	0.0013
Ch3	-2.9935	0.0009	-1.4555	0.0031	-0.2173	0.0015	-1.0356	0.0006	-1.5144	0.0026	-1.0553	0.0015
Ch4	-2.9999	0.0008	-1.4635	0.0030	-0.2222	0.0022	-1.0760	0.0009	-1.5490	0.0022	-1.0929	0.0013
Ch5	-3.0035	0.0009	-1.4670	0.0027	-0.2242	0.0019	-1.1106	0.0010	-1.5778	0.0019	-1.1249	0.0010
Ch6	-3.0082	0.0008	-1.4685	0.0030	-0.2304	0.0016	-1.1393	0.0009	-1.6032	0.0019	-1.1529	0.0011
Ch7	-3.0077	0.0006	-1.4723	0.0030	-0.2318	0.0017	-1.1651	0.0008	-1.6289	0.0021	-1.1808	0.0012

	Sheep 9											
	Healthy						**Adverse**					
	Pre	*Stdev*	*Max*	*Stdev*	*Post*	*Stdev*	*Pre*	*Stdev*	*Max*	*Stdev*	*Post*	*Stdev*
Precond.	--	--	--	--	-3.0851	0.0029	--	--	--	--	-2.1130	0.0016
Ch1	-2.9936	0.0005	-4.1956	0.0039	-3.1015	0.0054	-2.6651	0.0006	-3.2520	0.0049	-2.8295	0.0025
Ch2	-3.0726	0.0005	-4.2105	0.0030	-3.1164	0.0012	-2.8773	0.0004	-3.3383	0.0036	-2.9204	0.0017
Ch3	-3.0919	0.0006	-4.2199	0.0028	-3.1328	0.0033	-2.9537	0.0006	-3.3964	0.0028	-2.9815	0.0020
Ch4	-3.1041	0.0006	-4.2276	0.0026	-3.1371	0.0025	-3.0087	0.0004	-3.4468	0.0026	-3.0345	0.0018
Ch5	-3.1122	0.0006	-4.2335	0.0026	-3.1414	0.0007	-3.0570	0.0004	-3.4916	0.0021	-3.0778	0.0011
Ch6	-3.1172	0.0007	-4.2383	0.0027	-3.1461	0.0014	-3.0992	0.0005	-3.5298	0.0021	-3.1194	0.0017
Ch7	-3.1237	0.0005	-4.2407	0.0025	-3.1536	0.0016	-3.1382	0.0005	-3.5622	0.0020	-3.1553	0.0013

	Sheep 10											
	Healthy						**Adverse**					
	Pre	*Stdev*	*Max*	*Stdev*	*Post*	*Stdev*	*Pre*	*Stdev*	*Max*	*Stdev*	*Post*	*Stdev*
Precond.	--	--	--	--	-0.4667	0.0026	--	--	--	--	-1.2718	0.0016
Ch1	-0.3104	0.0010	-2.1202	0.0057	-0.6376	0.0057	-1.6930	0.0007	-2.2408	0.0028	-1.7753	0.0008
Ch2	-0.5899	0.0012	-2.1415	0.0057	-0.6660	0.0059	-1.8115	0.0008	-2.2943	0.0023	-1.8335	0.0012
Ch3	-0.6179	0.0010	-2.1589	0.0040	-0.6804	0.0039	-1.8609	0.0006	-2.3339	0.0019	-1.8760	0.0012
Ch4	-0.6387	0.0011	-2.1676	0.0040	-0.6992	0.0035	-1.9000	0.0008	-2.3675	0.0016	-1.9135	0.0011
Ch5	-0.6535	0.0016	-2.1764	0.0034	-0.7140	0.0069	-1.9336	0.0007	-2.3993	0.0021	-1.9479	0.0010
Ch6	-0.6643	0.0014	-2.1796	0.0050	-0.7149	0.0030	-1.9640	0.0011	-2.4263	0.0020	-1.9786	0.0017
Ch7	-0.6709	0.0012	-2.1871	0.0037	-0.7285	0.0048	-1.9911	0.0008	-2.4510	0.0017	-2.0018	0.0011

	Sheep 11											
	Healthy						**Adverse**					
	Pre	*Stdev*	*Max*	*Stdev*	*Post*	*Stdev*	*Pre*	*Stdev*	*Max*	*Stdev*	*Post*	*Stdev*
Precond.	--	--	--	--	-2.5901	0.0023	--	--	--	--	-0.7638	0.0018
Ch1	-2.4960	0.0017	-3.5932	0.0058	-2.6574	0.0081	-1.3312	0.0012	-1.9450	0.0044	-1.4617	0.0019
Ch2	-2.5976	0.0015	-3.6098	0.0041	-2.6722	0.0032	-1.5191	0.0012	-2.0227	0.0035	-1.5480	0.0017
Ch3	-2.6234	0.0021	-3.6198	0.0039	-2.6884	0.0043	-1.5888	0.0012	-2.0823	0.0028	-1.6113	0.0018
Ch4	-2.6404	0.0019	-3.6272	0.0041	-2.6998	0.0051	-1.6451	0.0013	-2.1309	0.0027	-1.6628	0.0015
Ch5	-2.6511	0.0018	-3.6314	0.0032	-2.7063	0.0039	-1.6920	0.0014	-2.1759	0.0030	-1.7081	0.0018
Ch6	-2.6620	0.0019	-3.6347	0.0041	-2.7120	0.0028	-1.7337	0.0010	-2.2138	0.0033	-1.7483	0.0016
Ch7	-2.6687	0.0019	-3.6397	0.0035	-2.7222	0.0049	-1.7745	0.0014	-2.2490	0.0042	-1.7895	0.0018

A.2 NP Pressure Data

Pressure data for pre-challenge (‘Pre’), challenge (‘Max’), and post-challenge (‘Post’) time points for healthy and adverse loading conditions, as acquired from processed sensor signals. Post-preconditioning pressure is a representative zero NP pressure for which super-hydration effects have been eliminated, but is not an absolute measurement of NP pressure. All pressure data is reported in MPa. Position data is not reported for tests that were stopped due to potting failure or other cases yielding an incomplete data set. Data is not reported for Sheep 1.

	Sheep 2											
	Healthy						**Adverse**					
	Pre	*Stdev*	*Max*	*Stdev*	*Post*	*Stdev*	*Pre*	*Stdev*	*Max*	*Stdev*	*Post*	*Stdev*
Precond.	--	--	--	--	0.6739	0.0251	--	--	--	--	0.4192	0.0112
Ch1	0.2773	0.0223	8.2059	0.0202	0.4629	0.0169	1.5645	0.0143	4.6963	0.0334	1.7032	0.0151
Ch2	0.4171	0.0189	8.1909	0.0144	0.5041	0.0214	1.5416	0.0138	4.2224	0.0097	1.6144	0.0127
Ch3	0.4352	0.0239	8.3470	0.0190	0.4937	0.0146	1.5119	0.0146	4.1900	0.0140	1.5568	0.0138
Ch4	0.4128	0.0337	8.1193	0.0178	0.4885	0.0261	1.4752	0.0113	4.1738	0.0067	1.5041	0.0129
Ch5	0.4034	0.0211	8.0800	0.0082	0.4689	0.0191	1.4342	0.0130	4.0943	0.0111	1.4926	0.0111
Ch6	0.3871	0.0216	8.0759	0.0127	0.4630	0.0245	1.4194	0.0154	4.0553	0.0111	1.4293	0.0218
Ch7	0.4006	0.0217	7.9337	0.0130	0.4623	0.0201	1.3940	0.0148	4.0048	0.0089	1.4270	0.0168

	Sheep 3											
	Healthy						**Adverse**					
	Pre	*Stdev*	*Max*	*Stdev*	*Post*	*Stdev*	*Pre*	*Stdev*	*Max*	*Stdev*	*Post*	*Stdev*
Precond.	--	--	--	--	0.2492	0.0410	--	--	--	--	--	--
Ch1	0.0634	0.0166	3.6649	0.0221	0.1303	0.0138	--	--	--	--	--	--
Ch2	0.1036	0.0152	3.7350	0.0185	0.1228	0.0115	--	--	--	--	--	--
Ch3	0.1562	0.0127	3.7362	0.0213	0.1469	0.0200	--	--	--	--	--	--
Ch4	0.1310	0.0182	3.7859	0.0168	0.1617	0.0206	--	--	--	--	--	--
Ch5	0.1554	0.0145	3.7865	0.0199	0.1962	0.0135	--	--	--	--	--	--
Ch6	0.2029	0.0166	3.7812	0.0159	0.2037	0.0147	--	--	--	--	--	--
Ch7	0.1662	0.0118	3.8017	0.0166	0.1994	0.0113	--	--	--	--	--	--

	Sheep 4											
	Healthy						**Adverse**					
	Pre	*Stdev*	*Max*	*Stdev*	*Post*	*Stdev*	*Pre*	*Stdev*	*Max*	*Stdev*	*Post*	*Stdev*
Precond.	--	--	--	--	0.2125	0.0097	--	--	--	--	0.6611	0.9538
Ch1	0.0535	0.0062	2.8966	0.0115	0.1347	0.0290	1.7105	0.0144	3.9357	0.0282	1.8069	0.0189
Ch2	-0.0056	0.0043	2.8952	0.0136	0.0759	0.0159	1.7197	0.0152	3.8844	0.0290	1.7872	0.0251
Ch3	-0.0257	0.0063	2.8868	0.0105	0.0348	0.0284	1.7200	0.0139	3.8135	0.0296	1.7731	0.0153
Ch4	-0.0482	0.0052	2.8729	0.0104	-0.0160	0.0369	1.7142	0.0188	3.7523	0.0344	1.7598	0.0193
Ch5	-0.0707	0.0053	2.8752	0.0092	-0.0195	0.0420	1.7033	0.0176	3.6809	0.0261	1.7374	0.0205
Ch6	-0.0794	0.0047	2.8596	0.0112	-0.0373	0.0359	1.6847	0.0218	3.6386	0.0271	1.7046	0.0201
Ch7	-0.0878	0.0068	2.8567	0.0096	-0.0539	0.0281	1.6689	0.0223	3.6111	0.0319	1.6815	0.0156

	Sheep 5											
	Healthy						**Adverse**					
	Pre	*Stdev*	*Max*	*Stdev*	*Post*	*Stdev*	*Pre*	*Stdev*	*Max*	*Stdev*	*Post*	*Stdev*
Precond.	--	--	--	--	-0.0728	0.0176	--	--	--	--	--	--
Ch1	-0.2803	0.0150	1.9869	0.0210	-0.1795	0.0281	--	--	--	--	--	--
Ch2	-0.3380	0.0121	2.0391	0.0128	-0.3071	0.0123	--	--	--	--	--	--
Ch3	-0.3297	0.0153	2.0678	0.0134	-0.3034	0.0167	--	--	--	--	--	--
Ch4	-0.3423	0.0149	2.0860	0.0151	-0.3125	0.0150	--	--	--	--	--	--
Ch5	-0.3445	0.0196	2.1062	0.0160	-0.3211	0.0270	--	--	--	--	--	--
Ch6	-0.3655	0.0134	2.1298	0.0194	-0.3283	0.0186	--	--	--	--	--	--
Ch7	-0.3564	0.0173	2.1394	0.0168	-0.3318	0.0131	--	--	--	--	--	--

	Sheep 6											
	Healthy						**Adverse**					
	Pre	*Stdev*	*Max*	*Stdev*	*Post*	*Stdev*	*Pre*	*Stdev*	*Max*	*Stdev*	*Post*	*Stdev*
Precond.	--	--	--	--	0.1672	0.0173	--	--	--	--	0.1581	0.0149
Ch1	-0.0196	0.0143	3.1910	0.0386	-0.0592	0.0177	0.9405	0.0173	2.4459	0.0209	0.9408	0.0144
Ch2	-0.0577	0.0159	3.1260	0.1054	-0.0751	0.0153	0.9442	0.0141	2.3220	0.0268	0.9441	0.0145
Ch3	-0.0706	0.0147	3.2005	0.0188	-0.0632	0.0146	0.9386	0.0121	2.2344	0.0331	0.9346	0.0171
Ch4	-0.0411	0.0195	3.1260	0.1054	-0.0222	0.0153	0.9237	0.0069	2.1713	0.0218	0.9258	0.0172
Ch5	-0.0375	0.0148	3.1260	0.1054	-0.0296	0.0164	0.9181	0.0134	2.1126	0.0173	0.9215	0.0126
Ch6	-0.0308	0.0190	3.1260	0.1054	-0.0220	0.0164	0.8913	0.0144	2.0630	0.0198	0.8941	0.0142
Ch7	-0.0147	0.0186	3.1260	0.1054	-0.0165	0.0155	0.8951	0.0154	2.0075	0.0162	0.8977	0.0156

	Sheep 7											
	Healthy						**Adverse**					
	Pre	*Stdev*	*Max*	*Stdev*	*Post*	*Stdev*	*Pre*	*Stdev*	*Max*	*Stdev*	*Post*	*Stdev*
Precond.	--	--	--	--	--	--	--	--	--	--	0.0320	0.0219
Ch1	--	--	--	--	--	--	1.1017	0.0196	3.1600	0.0167	1.1344	0.0183
Ch2	--	--	--	--	--	--	1.0924	0.0223	3.1210	0.0172	1.1226	0.0221
Ch3	--	--	--	--	--	--	1.0987	0.0232	3.1071	0.0206	1.1229	0.0265
Ch4	--	--	--	--	--	--	1.1073	0.0209	3.1064	0.0205	1.1221	0.0230
Ch5	--	--	--	--	--	--	1.0805	0.0193	3.0461	0.0217	1.0944	0.0241
Ch6	--	--	--	--	--	--	1.0562	0.0248	2.9867	0.0236	1.0799	0.0212
Ch7	--	--	--	--	--	--	1.0260	0.0147	2.9259	0.0232	1.0706	0.0253

	Sheep 8											
	Healthy						**Adverse**					
	Pre	*Stdev*	*Max*	*Stdev*	*Post*	*Stdev*	*Pre*	*Stdev*	*Max*	*Stdev*	*Post*	*Stdev*
Precond.	--	--	--	--	0.3743	0.0724	--	--	--	--	0.2671	0.0465
Ch1	0.1452	0.0702	3.4530	0.0811	0.2400	0.0544	1.2846	0.0544	3.1295	0.0566	1.4143	0.0552
Ch2	0.1844	0.0684	3.4821	0.0794	0.2181	0.0590	1.4034	0.0499	3.0745	0.0440	1.4440	0.0537
Ch3	0.2113	0.0613	3.4941	0.0831	0.2630	0.0810	1.3768	0.0495	3.0751	0.0773	1.4118	0.0548
Ch4	0.2642	0.0659	3.5537	0.0787	0.2486	0.0641	1.3853	0.0656	3.0221	0.0718	1.4003	0.0710
Ch5	0.2458	0.0586	3.5135	0.0620	0.2347	0.0638	1.3906	0.0499	2.9972	0.0576	1.4141	0.0662
Ch6	0.2591	0.0654	3.5226	0.0541	0.2474	0.0670	1.3879	0.0519	2.9979	0.0644	1.3878	0.0679
Ch7	0.2369	0.0468	3.5311	0.0635	0.2804	0.0644	1.3799	0.0577	2.9717	0.0729	1.3895	0.0664

	Sheep 9											
	Healthy						**Adverse**					
	Pre	*Stdev*	*Max*	*Stdev*	*Post*	*Stdev*	*Pre*	*Stdev*	*Max*	*Stdev*	*Post*	*Stdev*
Precond.	--	--	--	--	0.1370	0.0121	--	--	--	--	0.0956	0.0261
Ch1	0.1879	0.0092	3.5545	0.0124	0.3050	0.0127	1.8016	0.0307	2.8983	0.0311	1.8234	0.0276
Ch2	0.3558	0.0092	3.7043	0.0119	0.4294	0.0118	1.8310	0.0401	3.4978	0.0357	1.9740	0.0253
Ch3	0.3109	0.0079	3.6661	0.0108	0.3782	0.0104	2.2196	0.0346	3.5779	0.0454	2.2033	0.0277
Ch4	0.4214	0.0065	3.7687	0.0099	0.5147	0.0156	2.2827	0.0287	3.5121	0.0276	1.9548	0.0285
Ch5	0.3246	0.0105	3.6700	0.0112	0.3861	0.0115	1.9726	0.0230	3.6346	0.0364	1.7863	0.0288
Ch6	0.2799	0.0104	3.6215	0.0091	0.3611	0.0117	1.7921	0.0313	3.6327	0.0214	1.7732	0.0317
Ch7	0.2752	0.0078	3.6168	0.0110	0.3112	0.0107	1.8548	0.0212	3.6368	0.0249	1.8626	0.0254

	Sheep 10											
	Healthy						**Adverse**					
	Pre	*Stdev*	*Max*	*Stdev*	*Post*	*Stdev*	*Pre*	*Stdev*	*Max*	*Stdev*	*Post*	*Stdev*
Precond.	--	--	--	--	-0.0128	0.0203	--	--	--	--	0.2135	0.0212
Ch1	0.0945	0.0137	3.1618	0.0155	0.1253	0.0140	1.2146	0.0284	2.9907	0.0310	1.2502	0.0187
Ch2	0.1251	0.0170	3.2036	0.0168	0.1519	0.0122	1.2276	0.0221	2.9957	0.0241	1.2628	0.0191
Ch3	0.1450	0.0127	3.2257	0.0174	0.1642	0.0137	1.2197	0.0190	2.9940	0.0255	1.2418	0.0245
Ch4	0.1648	0.0175	3.2482	0.0200	0.1734	0.0130	1.1907	0.0173	2.9695	0.0287	1.2113	0.0207
Ch5	0.1669	0.0115	3.2724	0.0139	0.1993	0.0172	1.1701	0.0145	2.8971	0.0255	1.1880	0.0239
Ch6	0.1892	0.0119	3.2714	0.0242	0.2023	0.0125	1.1314	0.0187	2.8468	0.0358	1.1570	0.0208
Ch7	0.1914	0.0184	3.2909	0.0198	0.2190	0.0160	1.1110	0.0180	2.8183	0.0439	1.3956	0.2180

	Sheep 11											
	Healthy						**Adverse**					
	Pre	*Stdev*	*Max*	*Stdev*	*Post*	*Stdev*	*Pre*	*Stdev*	*Max*	*Stdev*	*Post*	*Stdev*
Precond.	--	--	--	--	0.1401	0.0124	--	--	--	--	0.2275	0.0118
Ch1	0.0816	0.0092	3.7190	0.0137	0.1164	0.0140	1.2279	0.0094	3.3638	0.0101	1.3087	0.0093
Ch2	0.0877	0.0105	3.8882	0.0167	0.1104	0.0117	1.2849	0.0110	3.3828	0.0129	1.3205	0.0101
Ch3	0.0845	0.0086	3.9031	0.0164	0.1171	0.0096	1.2872	0.0122	3.3528	0.0168	1.3140	0.0161
Ch4	0.0910	0.0131	3.9075	0.0160	0.1069	0.0131	1.2738	0.0081	3.3167	0.0148	1.2991	0.0128
Ch5	0.0917	0.0112	3.9199	0.0149	0.1158	0.0113	1.2583	0.0092	3.2737	0.0115	1.2787	0.0085
Ch6	0.0942	0.0120	3.9143	0.0127	0.1189	0.0109	1.2382	0.0117	3.2238	0.0133	1.2591	0.0116
Ch7	0.0936	0.0102	3.9298	0.0166	0.1189	0.0108	1.2216	0.0121	3.1749	0.0142	1.2341	0.0124

Bibliography

Adams, M. A., & Roughley, P. J. (2006). What is intervertebral disc degeneration, and what causes it? *Spine*, *31*(18), 2151–61. doi:10.1097/01.brs.0000231761.73859.2c

Adams, M., McNally, D., & Dolan, P. (1996). “Stress” distributions inside intervertebral discs the effects of age and degeneration. *Journal of Bone Joint Surgery*, *78B*, 965–972.

Antoniou, J., Steffen, T., Nelson, F., Winterbottom, N., Hollander, A. P., Poole, R. A., & Aebi, M. (1996). The Human Lumbar Intervertebral Disc. *Journal of Clinical Investigation*, *98*(4), 996–1003.

Bae, H., & Yu, M. (2012). Miniature Fabry-Perot pressure sensor created by using UV-molding process with an optical fiber based mold. *Optics Express*, *20*(13), 14573–83.

Buckwalter, J. A. (1995). Aging and Degeneration of the Human Intervertebral Disc. *Spine*, *20*(11), 1307-14.

Cassidy, J. J., Silverstein, M. S., Hiltner, A., & Baer, E. (1990). A water transport model for the creep response of the intervertebral disc. *Journal of Materials Science: Materials in Medicine*, *1*(2), 81–89. doi:10.1007/BF00839072

Cassinelli, E. H., & Kang, J. D. (2000). Current understanding of lumbar disc degeneration. *Operative Techniques in Orthopaedics*, *10*(4), 254–262. doi:10.1053/otor.2000.8400

Chan, S. C. W., Ferguson, S. J., & Gantenbein-Ritter, B. (2011). The effects of dynamic loading on the intervertebral disc. *European Spine Journal*, *20*(11), 1796–812. doi:10.1007/s00586-011-1827-1

Chin, K. K., Sun, Y., Feng, G., Georgiou, G. E., Guo, K., Niver, E., … Noe, K. (2007). Fabry-Perot diaphragm fiber-optic sensor. *Applied Optics*, *46*(31), 7614. doi:10.1364/AO.46.007614

Claus, A., Hides, J., Moseley, G. L., & Hodges, P. (2008). Sitting versus standing: does the intradiscal pressure cause disc degeneration or low back pain? *Journal of Electromyography and Kinesiology*, *18*(4), 550–8. doi:10.1016/j.jelekin.2006.10.011

Dakin, J. P., Wade, C. A., & Withers, P. B. (1987). An Optical Fibre Pressure Sensor. In *Proc SPIE 0734, Fibre Optics* (Vol. 0734, pp. 194–201).

De Schepper, E. I. T., Damen, J., van Meurs, J. B. J., Ginai, A. Z., Popham, M., Hofman, A., … Bierma-Zeinstra, S. M. (2010). The Association Between Lumbar Disc Degeneration and Low Back Pain: The Influence of Age, Gender, and Individual Radiographic Features. *Spine*, *35*(5).

Elliott, D., Yerramalli, C., Beckstein, J., Boxberger, J., Johannessen, W., & Vresilovic, E. (2008). The effect of relative needle diameter in puncture and sham injection animal models of degeneration. *Spine*, *33*(6), 588–96.

Heuer, F., Schmitt, H., Schmidt, H., Claes, L., & Wilke, H.-J. (2007). Creep associated changes in intervertebral disc bulging obtained with a laser scanning device. *Clinical Biomechanics (Bristol, Avon)*, *22*(7), 737–44. doi:10.1016/j.clinbiomech.2007.04.010

Hwang, D., Gabai, A. S., Yu, M., Yew, A. G., & Hsieh, A. H. (2012). Role of load history in intervertebral disc mechanics and intradiscal pressure generation. *Biomechanics and Modeling in Mechanobiology*, *11*(1-2), 95–106. doi:10.1007/s10237-011-0295-1

Iatridis, J., Weidenbaum, M., Setton, L., & Mow, V. (1996). Is the nucleus pulposus a solid or a fluid? Mechanical behaviors of the nucleus pulposus of the human intervertebral disc. *Spine*, *21*(10), 1174–1184.

Johannessen, W., Vresilovic, E. J., Wright, A. C., & Elliott, D. M. (2004). Intervertebral Disc Mechanics Are Restored following Cyclic Loading and Unloaded Recovery. *Annals of Biomedical Engineering*, *32*(1), 70–76.

Kepler, C. K., Ponnappan, R. K., Tannoury, C. A., Risbud, M. V, & Anderson, D. G. (2013). The molecular basis of intervertebral disc degeneration. *The Spine Journal : Official Journal of the North American Spine Society*, *13*(3), 318–30. doi:10.1016/j.spinee.2012.12.003

Lacroix, D., & Prendergast, P. J. (2002). A mechano-regulation model for tissue differentiation during fracture healing: analysis of gap size and loading. *Journal of Biomechanics*, *35*(9), 1163–1171. doi:10.1016/S0021-9290(02)00086-6

Livshits, G., Popham, M., Malkin, I., Sambrook, P. N., Macgregor, A. J., Spector, T., & Williams, F. M. K. (2011). Lumbar disc degeneration and genetic factors are the main risk factors for low back pain in women: the UK Twin Spine Study. *Annals of the Rheumatic Diseases*, *70*(10), 1740–5. doi:10.1136/ard.2010.137836

Long, M., & Rack, H. (1998). Titanium alloys in total joint replacement—a materials science perspective. *Biomaterials*, *19*(18), 1621–1639. doi:10.1016/S0142-9612(97)00146-4

MacLean, J. J., Lee, C. R., Alini, M., & Iatridis, J. C. (2005). The effects of short-term load duration on anabolic and catabolic gene expression in the rat tail intervertebral disc. *Journal of Orthopaedic Research : Official Publication of the Orthopaedic Research Society*, *23*(5), 1120–7. doi:10.1016/j.orthres.2005.01.020

MacPherson, W. N., Kilpatrick, J. M., Barton, J. S., & Jones, J. D. C. (1999). Miniature fiber optic pressure sensor for turbomachinery applications. *Review of Scientific Instruments*, *70*(3), 1868. doi:10.1063/1.1149682

Maroudas, A., Stockwell, R., Nachemson, A., & Urban, J. (1975). Factors involved in the nutrition of the human lumbar intervertebral disc: cellularity and diffusion of. *Journal of Anatomy*, *120*, 113–130.

McMillan, D. W., Garbutt, G., & Adams, M. A. (1996). Effect of sustained loading on the water content of intervertebral discs: implications for disc metabolism. *Annals of the Rheumatic Diseases*, *55*(12), 880–887. doi:10.1136/ard.55.12.880

Michalek, A. J., Buckley, M. R., Bonassar, L. J., Cohen, I., & Iatridis, J. C. (2011). The Effects of Needle Puncture Injury on Microscale Shear Strain in the Intervertebral Disc Annulus Fibrosus. *Spine*, *10*(12), 1098–1105. doi:10.1016/j.spinee.2010.09.015.The

Moon, S. M., Yoder, J. H., Wright, A. C., Smith, L. J., Vresilovic, E. J., & Elliott, D. M. (2013). Evaluation of intervertebral disc cartilaginous endplate structure using magnetic resonance imaging. *European Spine Journal*, *22*, 1820–8. doi:10.1007/s00586-013-2798-1

Nachemson, A. L., Schultz, A. B., & Berkson, M. H. (1979). Mechanical Properties of Human Lumbar Spine Motion Segments: Influences of Age, Sex, Disc Level, and Degeneration. *Spine*, *4*(1). 1-8.

Nesson, S., Yu, M., Zhang, X., & Hsieh, A. H. (2008). Miniature fiber optic pressure sensor with composite polymer-metal diaphragm for intradiscal pressure measurements. *Journal of Biomedical Optics*, *13*(4), 44040–44048.

O'Connell, G. D., Jacobs, N. T., Sen, S., Vresilovic, E. J., & Elliott, D. M. (2011). Axial creep loading and unloaded recovery of the human intervertebral disc and the effect of degeneration. *Journal of the Mechanical Behavior of Biomedical Materials*, *4*(7), 933–42. doi:10.1016/j.jmbbm.2011.02.002

O'Connell, G., Malhotra, N., Vresilovic, E., & Elliott, D. (2012). The Effect of Discectomy and the Dependence on Degeneration of Human Intervertebral Disc Strain in Axial Compression. *Spine*, *36*(21), 1765–1771. doi:10.1097/BRS.0b013e318216752f.The

O'Connell, G., Vresilovic, E., & Elliott, D. (2007). Comparison of animals used in disc research to human lumbar disc geometry. *Spine*, *32*(3), 328–333.

OpenStax CNX. (2014). Anatomy & Physiology. In *Human Anatomy & Physiology*.

Palmer, E. I., & Lotz, J. C. (2004). The compressive creep properties of normal and degenerated murine intervertebral discs. *Journal of Orthopaedic Research*, *22*, 164–169. doi:10.1016/S0736-0266(03)0Ol6l-X

Pei, B.-Q., Li, H., Li, D.-Y., Fan, Y.-B., Wang, C., & Wu, S.-Q. (2014). Creep bulging deformation of intervertebral disc under axial compression. *Bio-Medical Materials and Engineering*, *24*(1), 191–8. doi:10.3233/BME-130799

Poeggel, S., Tosi, D., Fusco, F., Mirone, V., Sannino, S., Lupoli, L., … Lewis, E. (2014). Fiber optic extrinsic Fabry-Perot interferometry pressure sensors for in-vivo urodynamic analysis. In *Proc SPIE 9157, 23rd International Conference on Optical Fibre Sensors* (Vol. 9157, pp. 915741–915744).

Reuber, M., Schultz, A., Denis, F., & Spencer, D. (1982). Bulging of Lumbar Intervertebral Disks. *Journal of Biomechanical Engineering*, *104*(3), 187–192.

Saar, G., Zhang, B., Ling, W., Regatte, R. R., Navon, G., & Jerschow, A. (2012). Assessment of glycosaminoglycan concentration changes in the intervertebral disc via chemical exchange saturation transfer. *NMR in Biomedicine*, *25*(2), 255–61. doi:10.1002/nbm.1741

Said, M. M., Radzi, S. A., Noh, Z. M., Junos, S. A. M., & Zabri, S. N. (2009). A New Diaphragm Material for Optical Fibre Fabry-Perot Pressure Sensor. *2009 Fifth International Conference on MEMS NANO, and Smart Systems*, 154–158. doi:10.1109/ICMENS.2009.15

Sato, K., Kikuchi, S., & Yonezawa, T. (1999). In Vivo Intradiscal Pressure Measurement in Healthy Individuals and in Patients With Ongoing Back Problems. *Spine*, *24*(23), 2468. doi:10.1097/00007632-199912010-00008

Sivan, S. S., Wachtel, E., & Roughley, P. (2014). Structure, function, aging and turnover of aggrecan in the intervertebral disc. *Biochimica et Biophysica Acta*, *1840*(10), 3181–9. doi:10.1016/j.bbagen.2014.07.013

Sivan, S., Neidlinger-Wilke, C., Würtz, K., Maroudas, A., & Urban, J. P. G. (2006). Diurnal fluid expression and activity of intervertebral disc cells. *Biorheology*, *43*, 283–291.

Smit, T. H. (2002). The use of a quadruped as an in vivo model for the study of the spine - biomechanical considerations. *European Spine Journal*, *11*(2), 137–44. doi:10.1007/s005860100346

Stokes, I. A. (1988). Bulging of Lumbar Intervertebral Discs: Non-contacting Measurements of Anatomical Specimens. *Journal of Spinal Disorders & Techniques*, *1*(3). 189-93.

Stokes, I. A. F., & Iatridis, J. C. (2004). Mechanical Conditions That Accelerate Intervertebral Disc Degeneration: Overload Versus Immobilization. *Spine*, *29*(23), 2724–2732. doi:10.1097/01.brs.0000146049.52152.da

Twomey, L., & Taylor, J. (1985). Age changes in lumbar intervertebral discs. *Acta Orthop Scand*, *56*(6), 496–499.

Vergroesen, P.-P. A, van der Veen, A. J., van Royen, B. J., Kingma, I., & Smit, T. H. (2014). Intradiscal pressure depends on recent loading and correlates with disc height and compressive stiffness. *European Spine Journal*, *23*(11), 2359–2368. doi:10.1007/s00586-014-3450-4

Walsh, A. J. L., & Lotz, J. C. (2004). Biological response of the intervertebral disc to dynamic loading. *Journal of Biomechanics*, *37*(3), 329–337. doi:10.1016/S0021-9290(03)00290-2

Walter, B. a, Korecki, C. L., Purmessur, D., Roughley, P. J., Michalek, A J., & Iatridis, J. C. (2011). Complex loading affects intervertebral disc mechanics and biology. *Osteoarthritis and Cartilage*, *19*(8), 1011–8. doi:10.1016/j.joca.2011.04.005

Wang, P., Yang, L., & Hsieh, A. H. (2011). Nucleus pulposus cell response to confined and unconfined compression implicates mechanoregulation by fluid shear stress. *Annals of Biomedical Engineering*, *39*(3), 1101–11. doi:10.1007/s10439-010-0221-1

Whatley, B. R., & Wen, X. (2012). Intervertebral disc (IVD): Structure, degeneration, repair and regeneration. *Materials Science and Engineering: C*, *32*(2), 61–77. doi:10.1016/j.msec.2011.10.011

Wilke, H. J., Kettler, A., Wenger, K. H., & Claes, L. E. (1997). Anatomy of the sheep spine and its comparison to the human spine. *The Anatomical Record*, *247*(4), 542–55.

Wilke, H., Neef, P., Caimi, M., Hoogland, T., & Claes, L. E. (1999). New In Vivo Measurements of Pressures in the Intervertebral Disc in Daily Life. *Spine*, *24*(8), 755–762. doi:10.1097/00007632-199904150-00005

Wolthuis, R. A., Mitchell, G. L., Saaski, E., Hartl, J. C., & Afromowitz, M. A. (1991). Development of Medical Pressure and Temperature Sensors Employing Optical Spectrum Modulation. *IEEE Transactions on Biomedical Engineering*, *38*(10), 974–981.

Wu, Y., Cisewski, S., Sachs, B., & Yao, H. (2013). Effect of cartilage endplate on cell based disc regeneration: a finite element analysis. *Molecular and Cellular Biomechanics*, *10*(2), 159–182.

Wuertz, K., Godburn, K., Maclean, J. J., Barbir, A., Stinnett, J., Roughley, P. J., … Iatridis, J. C. (2009). In Vivo Remodeling of Intervertebral Discs in Response to Short- and Long-Term Dynamic Compression. *Journal of Orthopaedic Research*, *27*(9), 1235–1242. doi:10.1002/jor.20867.In

Wuertz, K., Urban, J. P. G., Klasen, J., Ignatius, A., Wilke, H., & Claes, L. (2007). Influence of Extracellular Osmolarity and Mechanical Stimulation on Gene Expression of Intervertebral Disc Cells. *Journal of Orthopaedic Research*, *25*(11), 1513–1522. doi:10.1002/jor

Yu, C.-Y., Tsai, K.-H., Hu, W.-P., Lin, R.-M., Song, H.-W., & Chang, G.-L. (2003). Geometric and morphological changes of the intervertebral disc under fatigue testing. *Clinical Biomechanics*, *18*(6), S3–S9. doi:10.1016/S0268-0033(03)00078-0